

Influence of Mechanical Contrast and Confining Pressure on Fracture Behaviour in Layered Rocks

J. A. Regelink

Technische Universiteit Delft

Influence of Mechanical Contrast and Confining Pressure on Fracture Behaviour in Layered Rocks

By

Jacobus Albertus Regelink

in partial fulfillment of the requirements for the degree of

Master of Science
in Applied Earth Sciences

at the Delft University of Technology
to be defended publicly on Friday February 23, 2018 at 10:00 AM.

Supervisor: Dr. A. Barnhoorn
Thesis Committee: Prof. Dr. G. Bertotti
Dr. D.V. Voskov
L.A.N.R. Douma, MSc.

An electronic version of this thesis is available at <http://repository.tudelft.nl>



Preface

Before uploading my Master Thesis report to the infinite realm that is the TU Delft repository, I would like to take some time to thank everybody that has helped me in any way over the last year.

Firstly I would like to thank my supervisors Auke and Lisanne. You have taught me an awful lot about performing research, about being a researcher and how everything that you do has an implication on the results. I really enjoyed working together with you, spending many days in the laboratory performing experiments, enjoying lengthy discussions about the implications of our experimental results, or just having a good laugh.

Next I would like to thank the people from the Geoscience and Engineering laboratory, in particular Marc, Jens and Ellen. Who always took the time to help with sample preparation, setting up experiments, and visualizing the results.

Lastly I would like to thank my friends, family and everybody else who was there for me for the moral support. Although you didn't really help with the content of my research, you were there when I needed you.

Thanks everybody, it was a blast.

Jaap Regelink

Delft

February 15, 2018

Abstract

A rock fracture is a mechanical break or discontinuity that separates a rock body into two or more parts. The continuity or cohesion of the rock body is lost across a fracture. Fractures are formed in response to stress on a rock. A rock breaks and forms a fracture when the applied stress reaches the rock strength. Vertical fractures improve connectivity between multiple layers, and can aid the production of geothermal and petroleum reservoirs.

The heterogeneity of layered reservoirs leads to significant variation in mechanical properties, which in turn influence fracture nucleation, fracture growth and fracture geometry. This variation in rock mechanical properties, combined with layer thickness, is called mechanical stratigraphy. Natural fractures are subject to controls imposed by mechanical stratigraphy. Focusing on the mechanisms that control natural fracture development can improve fracture characterization. As rock strength is an important part of mechanical stratigraphy, the term mechanical contrast is introduced to examine the effect of contrasts in rock strength of adjacent layers.

This study examines the effect of the mechanical contrast and confining pressure on fracture behaviour in layered rocks in the laboratory. The focus of this study is threefold, it examines the effect of mechanical contrast and confining pressure on fracture propagation, fracture orientation and fracture aperture in layered rocks.

Unconfined and confined compressive strength tests have been performed on layered samples with varying mechanical contrasts at different confining pressures. A total of 169 tests have been performed which include confined and unconfined compressive strength tests on layered and monophasic samples and brazilian tensile strength tests and velocity measurements on monophasic samples.

The results show that fractures initiate in the weakest layer and propagate through the layer interface or are contained within the weakest layer. Unconfined compressive strength tests showed that differences in rock strength do not always act as a containment barrier.

The combination of mechanical contrast and confining pressure does control the containment of fractures within a layer. Lower horizontal compressive stresses are required to contain fractures when the mechanical contrast increases.

Mechanical contrast does not seem to influence fracture aperture. Confining pressure however greatly influences fracture aperture as it limits the ability of fractures to dilate.

Results show that fracture orientation is controlled by mechanical contrast. Fractures refract at layer interfaces when the mechanical contrast is sufficiently high. Confining pressure does not seem to affect the refraction of fractures.

The experimental results can improve the understanding of fracture containment, fracture aperture and fracture orientation in layered rocks at subsurface conditions. The mechanical contrast of the layered rocks, combined with the stress conditions need to be considered when characterizing subsurface fractures.

Vertical connectivity between layers is of importance when predicting fluid flow through reservoirs. As fractures often serve as preferential fluid flow paths, correctly interpreting fracture characteristics is important for successful development of layered reservoirs.

Contents

Preface	5
Abstract	7
1 Introduction	11
2 Methods & Materials	15
2.1 Rock mechanical parameters	15
2.1.1 Sample sizes	15
2.1.2 Matrix volume measurements	15
2.1.3 Young's modulus	16
2.1.4 Brazilian tensile strength	16
2.1.5 Ultrasonic velocities	17
2.2 Sample preparation	17
2.3 Materials	18
2.4 UCS test description	19
2.5 CCS test description	20
2.6 Correction of test data	21
2.7 Fracture analysis	21
3 Results	23
3.1 Fracture initiation	23
3.2 Fracture propagation and fracture containment	26
3.3 Fracture aperture	36
3.4 Fracture orientation	37
3.5 Fracture mode	39
3.6 Fracture step-over	40
4 Discussion	41
4.1 Initiation of fracture in weakest layer	41
4.2 Containment of fractures	41
4.3 Prediction of fracture propagation in the subsurface	42
4.4 Changes in fracture aperture	43
4.5 Changes in fracture orientation	44
5 Conclusion	45
6 Recommendations	47
Bibliography	49
Appendices	51
A List of experiments	52
B Fracture orientation change	55
C Ultrasonic traveltime measurements	58
D Brazilian tensile strength	61

Chapter 1

Introduction

A rock fracture is a mechanical break or discontinuity that separates a rock body into two or more parts. The continuity or cohesion of the rock body is lost across a fracture (Gudmundsson, 2011). Fractures are formed in response to stress on a rock. A rock breaks and forms a fracture when the applied stress reaches the rock strength (Gudmundsson, 2011). Vertical fractures can serve as high permeability pathways to transmit fluid flow (Wen et al., 2006). Connected fractures allow fluids to flow to wells, aiding the production of geothermal and petroleum reservoirs (Underwood et al., 2003; Ferrill et al., 2017).

Geothermal and petroleum reservoirs often consist of multiple lithological units with significant variation in mechanical properties (Passey et al., 2010). This heterogeneity affects fracture nucleation and growth (Roche et al., 2012), fault geometry and network characteristics (Ferrill and Morris, 2003; Morris et al., 2009). Heterogeneity of the lithology makes it difficult to correctly interpret fracture behaviour within a rock succession (Roche et al., 2012), as heterogeneity and anisotropy greatly influence fracture propagation (Brenner and Gudmundsson, 2004).

Accurate determinations of fracture characteristics are essential to characterizing permeability architecture (McGinnis et al., 2017). Predicting frequency and displacement characteristics represent an important component of fracture characterization (Morris et al., 2009). It is important to assess likely conditions at the time of fracturing in order to obtain defensible fracture interpretations and predictions (McGinnis et al., 2017). As fracture growth and its associated behaviour is a complex process (Roche et al., 2012), this study is limited to three attributes of fracture behaviour; fracture propagation, fracture aperture and fracture orientation.

Mechanical stratigraphy consists of the interplay between rock strength and layer thickness (Morris et al., 2009). Figure 1 shows an example of mechanical stratigraphy and its influence on fracture characteristics. Natural fractures are subject to controls imposed by mechanical stratigraphy, and focusing on the mechanisms that control natural fracture development can improve fracture characterizations (McGinnis et al., 2017). As rock strength is an important part of mechanical stratigraphy (Morris et al., 2009), the term mechanical contrast is introduced to examine the effect of contrasts in rock strength of adjacent layers.

Previous studies have shown that sharp contrasts in stiffness between layers are very effective in arresting the tips of fractures (Gudmundsson, 2002; Brenner and Gudmundsson, 2004). Fractures that nucleated within brittle layers are arrested in ductile layers as these tend to blunt the fracture tip (Gudmundsson, 2002; Ferrill et al., 2017). While most authors (Gudmundsson, 2002; Brenner and Gudmundsson, 2004; Ferrill et al., 2017) focused on stiffness contrast and corresponding ductile and brittle deformation behaviour, this study focuses on brittle deformation.

Discontinuities at contacts between rock layers with different mechanical properties are also of importance in fracture arrest (Gudmundsson and Brenner, 2001). Teufel and Clark (1984) suggested that a weak interfacial shear strength of the layers inhibits vertical growth of fractures in layered rocks. Teufel and Clark (1984) also suggested that differences in mechanical stratigraphy do not constitute an effective barrier per se. Contradicting the views of Gudmundsson (2002) and Brenner and Gudmundsson (2004). Remote loading of stiff layers may lead to the generation of stress barriers which inhibit fracture propagation (Teufel and Clark, 1984; Gudmundsson and Brenner, 2001; Brenner and Gudmundsson, 2004). Figure 2 shows an example of how fractures can be contained within layers, and how fractures can propagate through multiple layers.

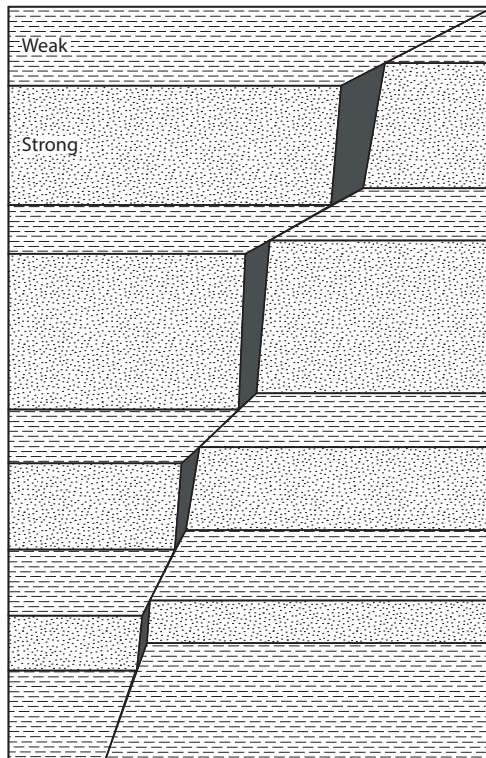


Figure 1: Mechanical stratigraphic model adapted from (Dunham, 1948). The image highlights the effect of mechanical stratigraphy, the interplay between the strength and thickness of the layers, and the influence on fracture characteristics such as fracture orientation and aperture.

Fractures that cut mechanically layered systems commonly have variable orientations (Roche et al., 2012; Ferrill et al., 2017). Variations in fracture orientation may be explained by variations in the local effective stress state (Ferrill and Morris, 2003; Roche et al., 2012), or can be related to the variable mechanical properties of the layers they cut (Ferrill and Morris, 2003; Ferrill et al., 2017). Refraction is also attributed to different modes of fracturing (Ferrill and Morris, 2003). Refracted fractures in layered segments consist of steeper segments in relatively stiffer and stronger layers, and more gently dipping segments in relatively weaker strata (Ferrill and Morris, 2003; Schöpfer et al., 2007; Ferrill et al., 2017). The direction of propagation (from strong to weak, or weak to strong strata) does not affect the fracture angle (Ferrill and Morris, 2003).

Fracture aperture depends on the mechanical properties of the host rocks (Brenner and Gudmundsson, 2004). Non-layered bound fractures show variation in aperture (Gillespie et al., 1999). Gillespie et al. (1999) suggest a statistical relationship between fracture distribution and fracture aperture, however no geological controls are suggested. Olson (2007) suggests a relation between fracture aperture and the amount of fractures. Fracture aperture will be higher for a system with a low fracture density, compared to a system with a high fracture density, as fewer fractures need to accommodate a certain strain (Olson, 2007). In a layered reservoir, layering is likely to affect the size of the aperture (Brenner and Gudmundsson, 2004). Field measurements indicate that fracture apertures tend to be greater in stiff layers than in the soft layers (Brenner and Gudmundsson, 2004). Mechanical stratigraphic controls on fracture aperture of non-strata bound fractures are not well documented. Brenner and Gudmundsson (2004) suggest that a reason for this might be that the change in aperture is too small to be noticed.

This study examines the effect of the mechanical contrast and confining pressure on fracture behaviour in layered rocks in the laboratory. The focus of this study is threefold, it examines the effects of mechanical contrast and confining pressure on fracture propagation, fracture orientation and fracture aperture in layered rocks. Unconfined and confined compressive strength tests have been performed on layered samples with varying mechanical contrasts at different confining pressures. With the experimental results we aim to provide insight into the influence of mechanical stratigraphy and confining pressure on fracture behaviour.

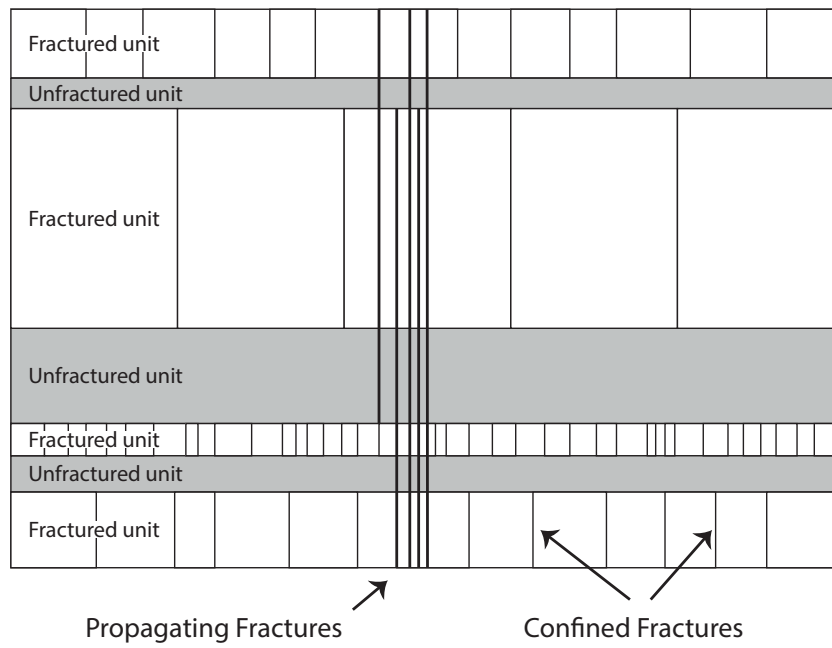


Figure 2: Mechanical stratigraphic model adapted from (Gross and Eyal, 2007). Fractures can either be confined in fractured layers, or propagate throughout several layers.

Chapter 2

Methods & Materials

2.1 Rock mechanical parameters

2.1.1 Sample sizes

Length and diameter of individual rock samples were measured three times, and measurement averages were computed. Average values were used in computations. Measurements were carried out with a caliper, with an accuracy of ± 0.05 mm.

Sample weight was measured once with a scale, with an accuracy of ± 0.01 g.

Bulk volume was calculated using equation (1). Bulk density was calculated using equation (2).

$$V_b = \pi \cdot \left(\frac{D}{2}\right)^2 \cdot L \quad (1)$$

Where V_b is the bulk volume in cm^3 .

D is the sample diameter in cm.

L is the sample length in cm.

$$\rho_b = m/V_b \quad (2)$$

Where ρ_b is the bulk density in g/cm^3 .

V_b is the bulk volume in cm^3 .

m is the sample weight in g.

2.1.2 Matrix volume measurements

Matrix volume was measured using a *Quantachrome Ultrapycnometer 1000*, measurements were carried out until the deviation between the last three measurements was within $\pm 0.005\%$. The accuracy of measurements is $\pm 0.0001 \text{ cm}^3$.

The working principle of the pycnometer is based on Boyle's Law. A constant volume of Helium gas is injected into a cell with known volume. Placing an object into the cell changes the volume, and a different pressure is reached when a constant volume of gas is injected. From the difference in cell pressure, the object's volume can be calculated. If the test subject is a porous rock sample, the matrix volume is measured. Matrix density and effective porosity were calculated with equations (3) and (4) respectively.

$$\rho_{ma} = m/V_{ma} \quad (3)$$

Where ρ_{ma} is the matrix density in g/cm^3 .

m is the sample weight in g.

V_{ma} is the matrix volume in cm^3 .

$$\phi = \frac{V_b - V_{ma}}{V_b} \quad (4)$$

Where ϕ is the sample's porosity, dimensionless.

V_{ma} is the matrix volume in cm^3 .

V_b is the bulk volume in cm^3 .

2.1.3 Young's modulus

The Young's modulus is a measure of stiffness of a material. It is determined from the recorded stress and strain during unconfined compressive strength (UCS) tests. A representative reading of the stress and strain in the elastic regime is taken. Figure 3 shows the stress-strain curve for a Red Felser sandstone sample. The elastic regime is at intermediate stress and strain. At a low stress and strain, closure of pre-existing micro-cracks leads to non-linear behaviour. At high stress and strain, fracture initiation leads to non-linear behaviour.

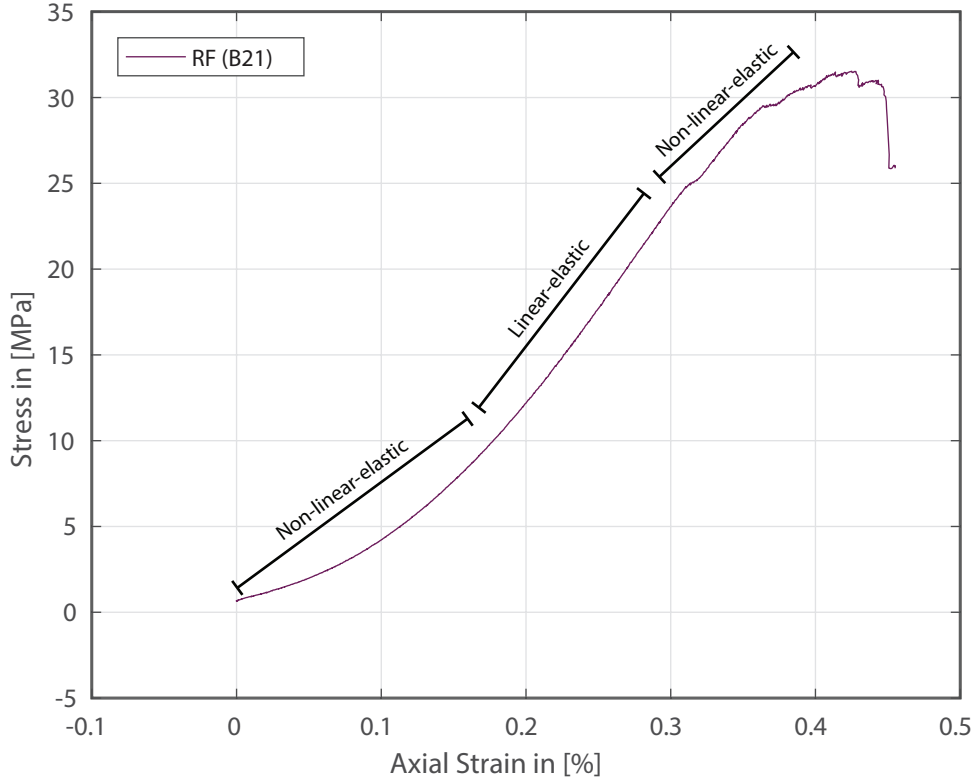


Figure 3: Stress-strain curve of Red Felser sandstone sample. Regions with linear-elastic and non-linear-elastic behaviour are shown.

During unconfined and confined compressive strength tests, the strain in a rock sample is related to the applied stress on a rock sample through the Young's modulus. This relation is given by Hooke's Law, equation (5). The displayed Young's modulus is an average value, calculated from several UCS tests.

$$E = \frac{\sigma}{\epsilon} \quad (5)$$

Where E is the Young's modulus in GPa.

σ is the axial stress in MPa.

ϵ is the axial strain, dimensionless.

Equation (5) is valid under the assumptions that the material is homogeneous and isotropic, that the relation between stress and strain is linear, that strains are infinitesimal and that the rock becomes instantaneously strained when stress is applied (Gudmundsson, 2011).

2.1.4 Brazilian tensile strength

The Brazilian test is a widely used tool in the industry to indirectly obtain the tensile strength of a rock. By compressing a circular disc to failure, indirect tensile stress is induced on the sample (ISRM, 1978).

Brazilian Disc tests were performed to obtain their Brazilian Tensile Strength (BTS). The tests were performed using a high-strength steel jig, in a 50kN load frame. Displacement was measured by two linear variable displacement transformers (LVDT's).

The samples were deformed in times ranging from 30 seconds to 2 minutes, at various speeds ranging from a displacement rate of 0.0008 1/s to 0.003 1/s.

The BTS can be calculated using equation (6).

$$\sigma_t = \frac{2P}{\pi Dt} \quad (6)$$

Where σ_t is the brazilian tensile strength in MPa.

P is the peak load at failure in kN.

D is the sample diameter in mm.

t is the sample thickness in mm.

2.1.5 Ultrasonic velocities

Traveltimes of ultrasonic compressional (P) and shear (S) waves through rock samples were measured. 1Mhz P- and S-wave transducers and receivers were used, and propagated waves were visualized with a Yokogawa oscilloscope. P- and S-wave velocities were calculated from the measured traveltimes. No stress was applied during measurements.

The dynamic Poisson's Ratio can be calculated by using the P- and S-wave velocities through equation (7), based on the elastic wave equation, e.g. (Mavko et al., 2003).

$$\nu = \frac{1}{2} \frac{V_p^2 - 2V_s^2}{V_p^2 - V_s^2} \quad (7)$$

Where ν is the Poisson's ratio, dimensionless.

V_p is the pressure wave velocity in m/s.

V_s is the shear wave velocity in m/s.

2.2 Sample preparation

Cylinders with a diameter of 29 mm were cored with a hydraulically controlled, water cooled drill, from large blocks of rock. These cylinders are measured on straightness and subsequently cut into pieces with a length of 20 mm or 60 mm with a diamond blade.

The end surfaces are sanded with a 125 μm grit until sufficient parallelity is obtained. The difference should be within $1/10^{\text{th}}$ of a millimeter. Surfaces are also sanded to obtain the same roughness. After these steps, the samples are dried in an oven at 50 °C for a minimum of 24 hours.

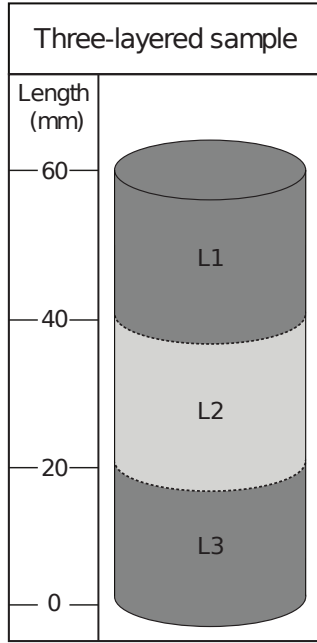
Two types of samples were used, monolithic samples that consist of one piece of rock, and three-layered samples that consist of two types of rock. The individual samples have a 29 mm diameter and 60 mm length. The components that make up the synthetically layered samples have a 29 mm diameter and 20 mm length, such that the composite samples have a total length of 60 mm.

Used sample dimensions are based on a 1 : 2 diameter-length ratio prescribed by test standard [ASTM D2938-95 \(1995\)](#) and on equipment dimensions.

The composite samples always consist of two different rock types with different unconfined compressive strength. The top and bottom layers are of the same rock type and have the same strength, but differ in strength from the middle layer. This difference in rock strength between the strongest and weakest rock layers results in a contrast in strength, which is called the mechanical contrast.

By varying lithologies, sample configurations with various mechanical contrasts were obtained. Combinations were made in order to obtain a spread as large as possible in mechanical contrast.

A schematic overview of a layered test sample is shown in Figure 4(a), and a photo of a layered sample is shown in Figure 4(b). Experiments were performed on synthetically layered samples with configurations as shown in Table 1. The strength of the individual components, and the mechanical contrast of the samples are shown in Table 1.



(a) Schematic overview of a synthetically layered sample. L1 refers to layer 1, L2 to layer 2, L3 to layer 3.

(b) Photo of synthetically layered sample. Sample consists of Red Felsler sandstone as top and bottom layer, and Bentheim sandstone as middle layer.

Figure 4

Layer 1	AIN	RF	BNT	AIN	BNT	RF	AIN
UCS (MPa)	203.5 ± 10.8	31.4 ± 3.9	42.7 ± 0.9	203.5 ± 10.8	42.7 ± 0.9	31.4 ± 3.9	203.5 ± 10.8
Layer 2	GRA	BNT	BER	BNT	GRA	GRA	SLT
UCS (MPa)	222.1 ± 21.2	42.7 ± 0.9	125.7 ± 17.4	42.7 ± 0.9	222.1 ± 21.2	222.1 ± 21.2	13
Layer 3	AIN	RF	BNT	AIN	BNT	RF	AIN
UCS (MPa)	203.5 ± 10.8	31.4 ± 3.9	42.7 ± 0.9	203.5 ± 10.8	42.7 ± 0.9	31.4 ± 3.9	203.5 ± 10.8
M.C.	1.1	1.4	2.9	4.8	5.2	7.1	15.8

Table 1: Sample configurations, component strength and their corresponding mechanical contrast (M.C.). BNT: Bentheim sandstone, BER: Beringen sandstone, AIN: Ainsa sandstone, RF: Red Felsler sandstone, GRA: Benin granite, SLT: Huesca siltstone.

2.3 Materials

The individual samples and components of the three-layered samples were sourced from six different lithologies with varying material properties. A physical description of the rocks is displayed in Table 2. The rock mechanical parameters are displayed in Table 3. Material properties were obtained from tests performed on individual samples (60 mm length, 29 mm diameter). The lithologies include various sandstones, because alternating sandstone layers are commonly found in hydrocarbon reservoirs. Granite and siltstone are used as components to create extreme mechanical contrasts. Although configurations with such high mechanical contrasts are not commonly found in the subsurface.

	Matrix Density (kg/m^3)	Porosity (-)	Description
BNT	2.6635 ± 0.0044	0.2495 ± 0.0058	Sandstone, yellow/white color, friable, very porous
BER	2.6900 ± 0.0059	0.0857 ± 0.0198	Sandstone, light grey color, clear layering, dykes, clay-rich, fine-grained
AIN	2.7037 ± 0.0039	0.0169 ± 0.0024	Sandstone, dark grey color, calcite-cemented, turbidite, tight, fine-grained
RF	2.6563 ± 0.0069	0.2136 ± 0.0030	Sandstone, red/pink color, friable, very porous, quartz-rich
GRA	2.6407 ± 0.0042	0.0079 ± 0.0020	Granite, granular texture, predominantly white, white/grey orthoclase
SLT	-	-	Siltstone, yellow/brown color, very friable, mud-rich, very fine grained

Table 2: Physical description of lithologies used in laboratory experiments. Matrix density and porosity values of BNT and GRA courtesy of [Janmahomed \(2016\)](#). BNT: Bentheim sandstone, BER: Beringen sandstone, AIN: Ainsa sandstone, RF: Red Felser sandstone, GRA: Benin granite, SLT: Huesca siltstone.

	Youngs Modulus (GPa)	P-wave velocity (m/s)	S-wave velocity (m/s)	Unconfined Compressive Strength (MPa)	Brazilian Tensile Strength (MPa)	Poisson's Ratio (-)
BNT	9.09 ± 2.42	2315 ± 76	1597 ± 58	42.7 ± 0.9	3.17 ± 0.47	0.206 ± 0.038
BER	19.95 ± 3.12	-	-	125.7 ± 17.4	-	0.105 ± 0.017
AIN	29.49 ± 7.64	4960 ± 35	3107 ± 28	203.5 ± 10.8	14.96 ± 1.57	0.154 ± 0.012
RF	7.15 ± 3.05	2277 ± 116	1518 ± 72	31.4 ± 3.9	2.46 ± 0.30	0.125 ± 0.037
GRA	30.82 ± 3.16	4849 ± 369	3182 ± 204	222.1 ± 21.2	-	0.181 ± 0.018
SLT	2.2	-	-	13	-	-

Table 3: Rock mechanical properties of lithologies used in laboratory experiments. Poisson's ratio data for BNT and GRA courtesy of [Janmahomed \(2016\)](#). BNT: Bentheim sandstone, BER: Beringen sandstone, AIN: Ainsa sandstone, RF: Red Felser sandstone, GRA: Benin granite, SLT: Huesca siltstone.

2.4 UCS test description

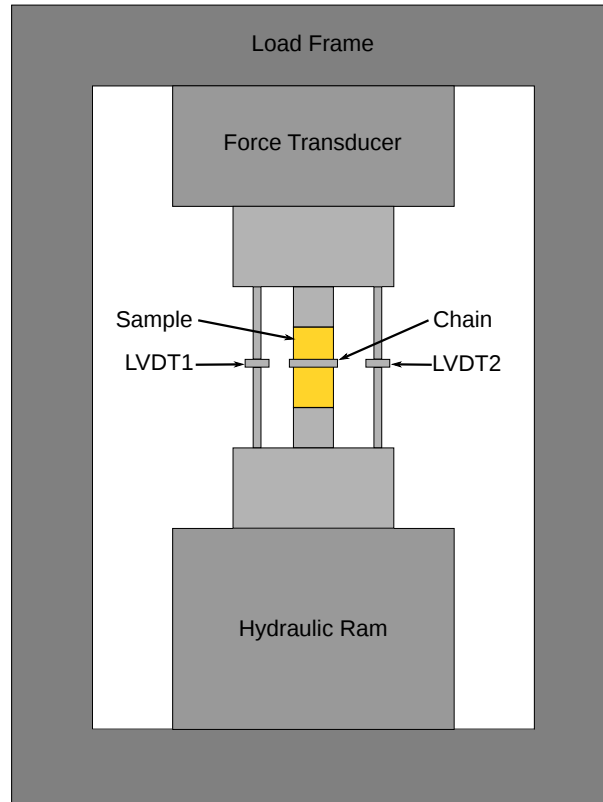


Figure 5: Schematic overview of the UCS test setup.

Unconfined compressive strength (*UCS*) tests were performed on individual rock samples to obtain their ultimate strength, Young’s modulus and Poisson’s ratio. *UCS* tests were also performed on composite layered samples to obtain the ultimate strength of the layered system and to investigate the influence of mechanical contrast on fracture behaviour at unconfined conditions.

Figure 5 shows a schematic overview of the experimental setup. The samples were placed in a pressure bench with a 500 kN load frame. A hydraulic ram provides force on the sample.

The sample is deformed until failure, to create stress-driven fractures, and to obtain the samples ultimate strength.

Axial strain is recorded by linear variable displacement transformers. The sample is loaded at a constant displacement rate of 0.0006 mm/s, corresponding to a strain rate of 10^{-5} s^{-1} . An extensometer measures the change in chain length. Radial strain is calculated from the change in chain length. The experiments were carried out at room temperature ($\sim 20 \text{ }^\circ\text{C}$).

2.5 CCS test description

Confined compressive strength (*CCS*) tests were performed on layered rock samples to obtain the ultimate strength of the composite sample at different confining pressure conditions. And to investigate the influence of confining pressure and mechanical contrast on fracture behaviour.

Figure 6 shows a schematic overview of the experimental setup. The same setup as for the *UCS* was used, but a confining pressure is applied using a triaxial Hoek cell (Hoek and Franklin, 1968). Pressure is kept constant during the test, a Teledyne ISCO pump was used. The sample is deformed until failure, to create a stress-driven fractures. Loading was halted when the stress approached a constant value after failure.

Axial strain is recorded using linear variable displacement transformers, the sample is loaded at a constant displacement rate of 0.0006 mm/s, corresponding to a strain rate of 10^{-5} s^{-1} . The experiments were carried out at room temperature ($\sim 20 \text{ }^\circ\text{C}$).

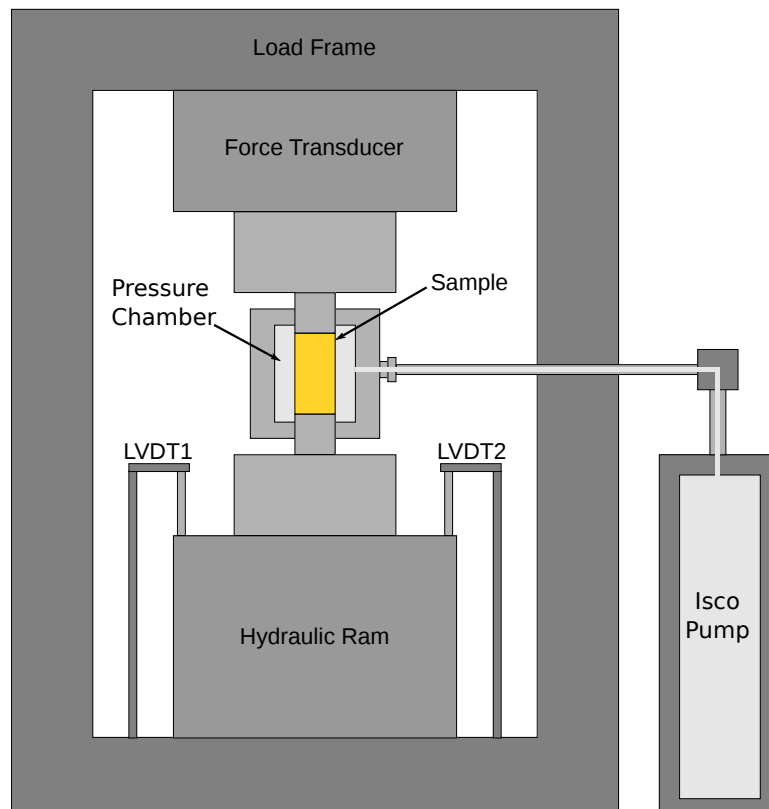


Figure 6: Schematic overview of the CCS test setup.

2.6 Correction of test data

A correction is applied to the stress and strain data obtained from UCS and CCS tests. The test setups contain many high strength steel elements which also deform during the experiments. The dimensions of high strength steel components were measured, and elastic strain in the steel elements is calculated based on the material's Young's modulus of 210 GPa, using equation (8).

$$\epsilon_{steel} = \frac{\sigma}{E_{steel}} \quad (8)$$

Where ϵ_{steel} is the strain in the steel parts, dimensionless.

σ is the applied stress in MPa.

E_{steel} is the Young's modulus of the steel parts in GPa.

The total amount of strain is a sum of the strain in the steel parts and the strain in the rock. The amount of strain in the rock sample is obtained by subtracting the amount of strain in the steel parts by using equation (9).

$$\epsilon_{rock} = \epsilon_{total} - \epsilon_{steel} \quad (9)$$

Figure 7 shows a graph with the original stress-strain data and the corrected stress-strain data.

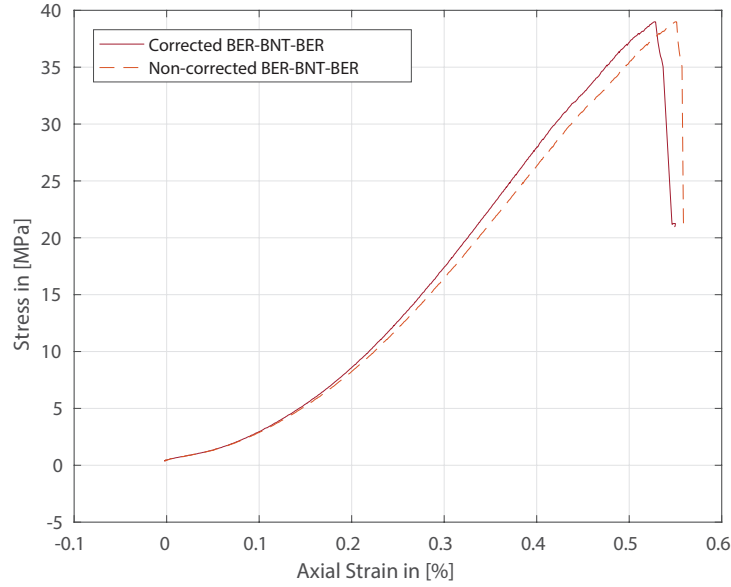


Figure 7: Original stress-strain curve of BER-BNT-BER sample, and the corrected stress-strain curve.

2.7 Fracture analysis

The stress-driven fractures were visualized using the *Nanotom X-ray micro computed tomography* (micro-CT) scan (resolution 30 μm). This technique uses X-rays to create a three-dimensional dataset of a sample by stacking cross-sectional two-dimensional images. The principles are described by Wellington and Vinegar (1987).

The created datasets were analyzed using *myVGL 3.0 SP4* software from Volume Graphics (2017), to characterize fracture containment, propagation and geometry in the three-layered samples.

Chapter 3

Results

Unconfined and confined compressive tests were performed on individual and three-layered samples. The test results were analyzed by using micro-CT scans of the samples to identify fracture propagation, fracture arrest, and fracture containment. Micro-CT scans were also used to describe fracture geometry.

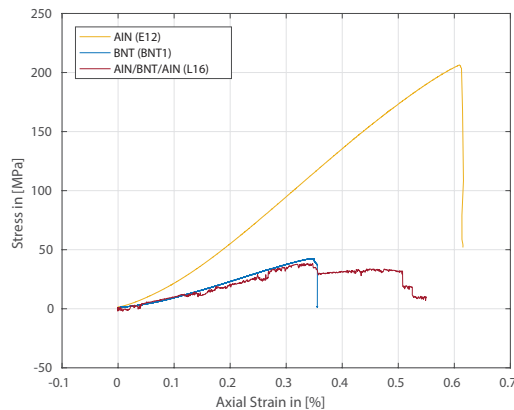
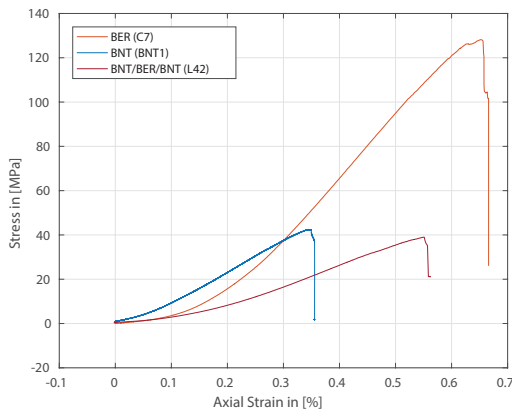
The first section deals with the initiation of stress-driven fractures in individual and layered test samples. The second section focuses on the influence of mechanical contrast and confining pressure on fracture propagation and containment in test samples. Section three focuses on the change in fracture aperture, whereas section four focuses on changes in fracture orientation.

3.1 Fracture initiation

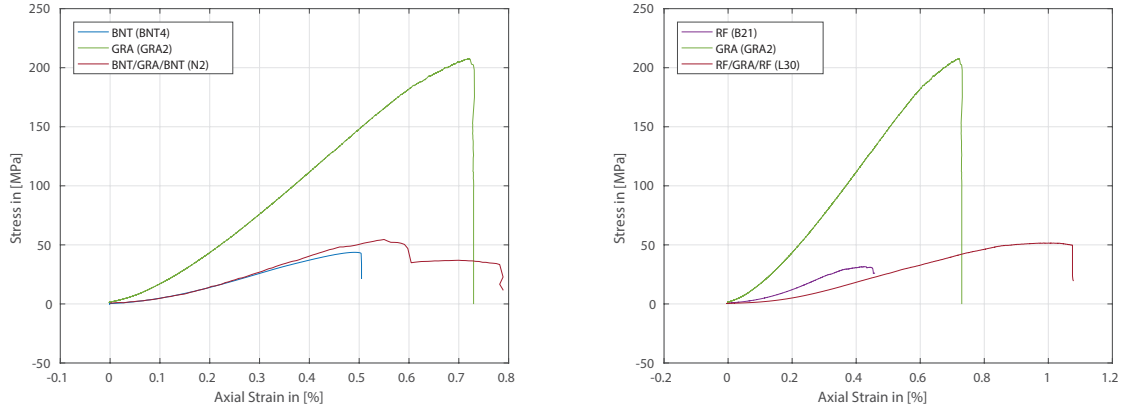
Figure 8 contains four graphs with stress-strain curves. Each graph contains the stress-strain curve of two individual rock samples, and a layered sample consisting of these two rocks.

Figure 8(a) shows that the individual sample of Beringen sandstone fails at ~ 128 MPa, and the individual Bentheim sandstone sample fails at ~ 39 MPa. The layered sample consisting of Bentheim sandstone and Beringen sandstone, L42, fails at ~ 39 MPa. So the individual Bentheim sandstone sample, and the layered sample containing Bentheim sandstone both fail at roughly ~ 40 MPa. The strength difference between the individual rocks results in a mechanical contrast of 2.9.

A second set of stress-strain curves is displayed in figure 8(b). It shows that the individual sample of Ainsa sandstone fails at roughly ~ 206 MPa, whilst the individual Bentheim sandstone sample fails at ~ 42 MPa. The layered sample consisting of Ainsa sandstone and Bentheim sandstone, L16, fails at ~ 38 MPa. The individual Bentheim sandstone sample, and the layered sample containing Bentheim sandstone both fail at roughly ~ 40 MPa. The strength difference between the individual rocks results in a mechanical contrast of 4.8.



(a) BER: Beringen sandstone, BNT: Bentheim sandstone
(b) AIN: Ainsa sandstone, BNT: Bentheim sandstone



(c) BNT: Bentheim sandstone, GRA: Benin granite (d) RF: Red Felsler sandstone, GRA: Benin granite

Figure 8: Stress-strain curves for individual samples and layered samples with various mechanical contrasts at unconfined conditions. (a) individual BER and BNT samples, layered sample consisting of BNT and BER. (b) individual AIN and BNT samples, layered sample consisting of AIN and BNT. (c) individual BNT and GRA samples, layered sample consisting of BNT and GRA. (d) individual RF and GRA samples, layered sample consisting RF and GRA. N2 test data courtesy of [Janmahomed \(2016\)](#), BNT and GRA data courtesy of [Zotz-Wilson \(2016\)](#).

Figure 8(c) shows that the individual sample of Bentheim sandstone fails at ~ 43 MPa, and the individual Benin granite sample fails at roughly ~ 207 MPa. The layered sample consisting of Bentheim sandstone and Benin granite, N2, fails at roughly ~ 54 MPa. There is a slight difference in yield stress between the layered sample, and the individual Bentheim sandstone sample. However, the yield stress of the layered sample is much closer to the yield stress of the individual Bentheim sandstone sample than that of the individual Benin granite sample. The strength difference between the individual rocks results in a mechanical contrast of 5.2.

The fourth set of stress-strain curves is displayed in figure 8(d). It shows that the individual sample of Red Felsler sandstone fails at ~ 31 MPa. The individual Benin granite sample fails at ~ 207 MPa. The layered sample consisting of Red Felsler sandstone and Benin granite, L30, fails at ~ 51 MPa. There is a difference of ~ 20 MPa in yield stress for the layered sample and the individual Red Felsler sandstone sample. The yield point of the layered sample is however closer to that of the Red Felsler sandstone sample instead of the Benin granite sample. The strength difference between the individual rocks results in a mechanical contrast of 7.1. Analysis of the layered sample after the experiment showed an eroded base, which may be caused by improper alignment and insufficient parallelity of the sample top and base. The erosion of the top may have caused the strain to be nearly 2.5 times as high, when compared to the individual Red Felsler sandstone sample.

The difference in yield stress for the layered samples, compared to the yield stress of their weakest constituent, is for figures 8(a) - 8(d) respectively 8%, 10%, 26% and 65%. The difference in yield stress for the layered samples, compared to the yield stress of their strongest constituent, is for figures 8(a) - 8(d) respectively 328%, 542%, 383% and 405%.

As the yield stress of the layered sample is much closer to the yield stress of its weakest constituent compared to its strongest constituent, fracture initiation is likely to occur in the weakest layer of the layered sample. This behaviour is observed for mechanical contrasts ranging from 2.9 to 7.1, making it likely that fracture initiation occurs in the weakest layer, irrespective of the mechanical contrast, at unconfined pressure conditions.

Figure 9(a) shows the ultimate strength values of layered samples with varying mechanical contrasts at different confining pressures. The curve for the samples with Ainsa sandstone as the weakest constituent ($MC = 1.1$) is consequently around 100 MPa higher than the others. The other curves, for samples with mechanical contrasts ranging from 1.4 - 7.1 all have similar ultimate strengths. Samples with different mechanical contrasts, but with the same weakest material all fail roughly at the same stress, for different confining pressures. Thus making it likely that fracture initiation also occurs in the weakest material for confined pressure conditions.

The Young's modulus of layered samples with various mechanical contrasts at different confining pressures is shown in Figure 9. While samples with the same weakest material fail at the same stress, as shown in Figure 9(a), the Young's modulus of these samples differs with approximately 7.5 GPa. The graph clearly shows that samples with higher mechanical contrasts have higher Young's moduli, which indicates that stronger layers take up more strain at higher contrasts.

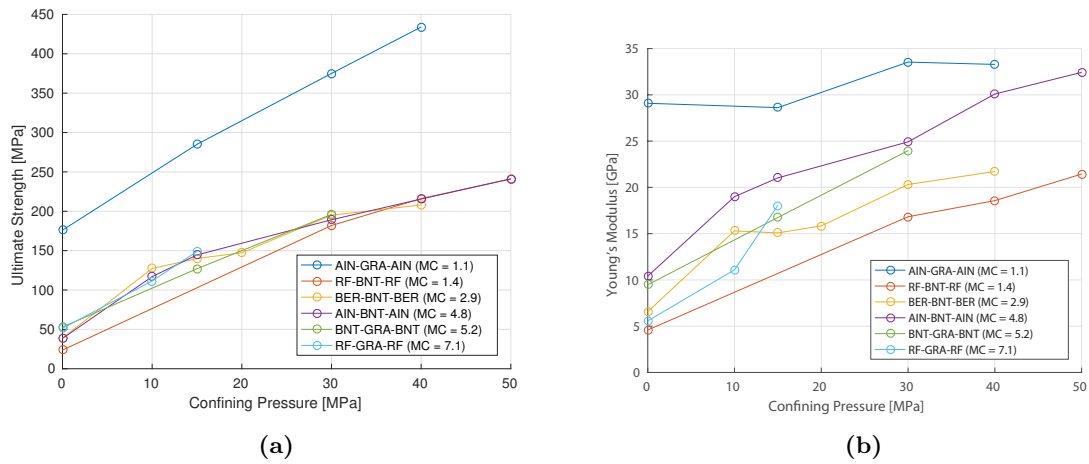


Figure 9: (a) Ultimate strength of layered samples with different mechanical contrasts at different confining pressures. (b) Young's modulus of layered samples with different mechanical contrasts at different confining pressures.

Analysis of the ultimate strength of layered samples at unconfined conditions showed that layered samples do not always fail at the expected stress. Figure 10(a) shows the strength contrasts between the strongest and weakest material, and the layered sample consisting of both materials. The blue bar shows the ratio between the ultimate strength of the weakest material and the layered sample. A value close to one (dotted line), means that the ultimate strength of the weakest material is the same as the layered sample, indicating fracture initiation in the weakest layer.

For mechanical contrasts ranging from 5.2 - 17.0, the strength of the layered sample exceeds the strength of the weakest material, indicating strength reinforcement for high mechanical contrasts due to mechanical layering. Analysis of the Young's modulus in Figure 10(b) shows that the Young's modulus increases for contrasts ranging from 3.2 - 4.3, indicating a higher resistance to deformation, due to the mechanical layering.

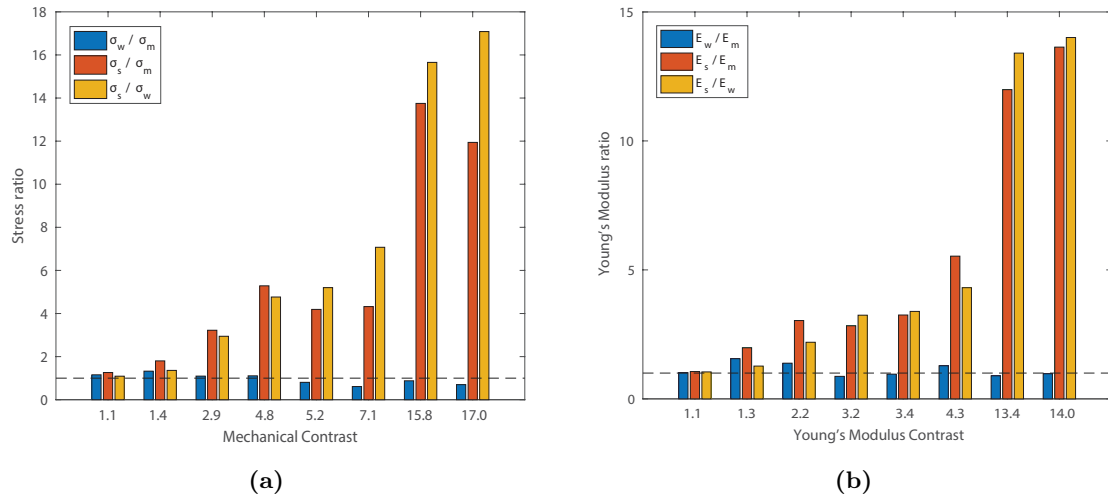


Figure 10: (a) Different strength ratio's for varying mechanical contrasts. In blue, strength ratio between the weakest material and the layered sample. In red, strength ratio between the strongest material and the layered sample. In yellow, strength ratio between the strongest and weakest material (mechanical contrast). (b) Different Young's modulus ratio's for varying mechanical contrasts. In blue, Young's modulus ratio between the weakest material and the layered sample. In red, Young's modulus ratio between the strongest material and the layered sample. In yellow, strength ratio between the strongest and weakest material.

3.2 Fracture propagation and fracture containment

Unconfined experiments were carried out to create stress driven fractures in rock samples. Micro-CT scans were used to visualize the fracture patterns in these test samples.

Figure 11 shows micro-CT images of six different test samples. The samples consist of different rock combinations, and thus have different mechanical contrasts ranging from 1.1 – 7.1. All samples were deformed at unconfined pressure conditions.

Annotations are made to highlight fracture containment and fracture propagation.

Figure 11(a) shows a micro-CT slice of a sample consisting of Ainsa sandstone and Benin granite. Ainsa sandstone is the weakest rock in this combination, while Benin granite is the strongest. The strength difference between these rocks results in a mechanical contrast of 1.1. A shear fracture initiates in the Ainsa sandstone layer at the bottom of the sample and propagates through the interface into the granite layer in the middle, and is arrested at the other sandstone/granite interface.

Figure 11(b) shows a micro-CT slice of a sample consisting of Red Felsler sandstone and Bentheim sandstone, with Red Felsler sandstone being the weakest constituent. The strength difference between these rocks results in a mechanical contrast of 1.4. A shear fracture initiates in the Red Felsler sandstone layer at the top, and propagates through the interface into the Bentheim layer in the middle. The fracture splits into two parts, both of them being arrested at the bottom of the Bentheim layer.

Figure 11(c) shows a micro-CT slice of a sample consisting of Bentheim sandstone and Beringen sandstone. Bentheim sandstone is the weakest rock in this combination, and Beringen sandstone is the strongest rock in this combination. Their strength difference results in a mechanical contrast of 2.9. A shear fracture is initiated in the weaker Bentheim layer at the bottom of the sample, and propagates into the Beringen layer. The fracture is arrested at the other rock interface.

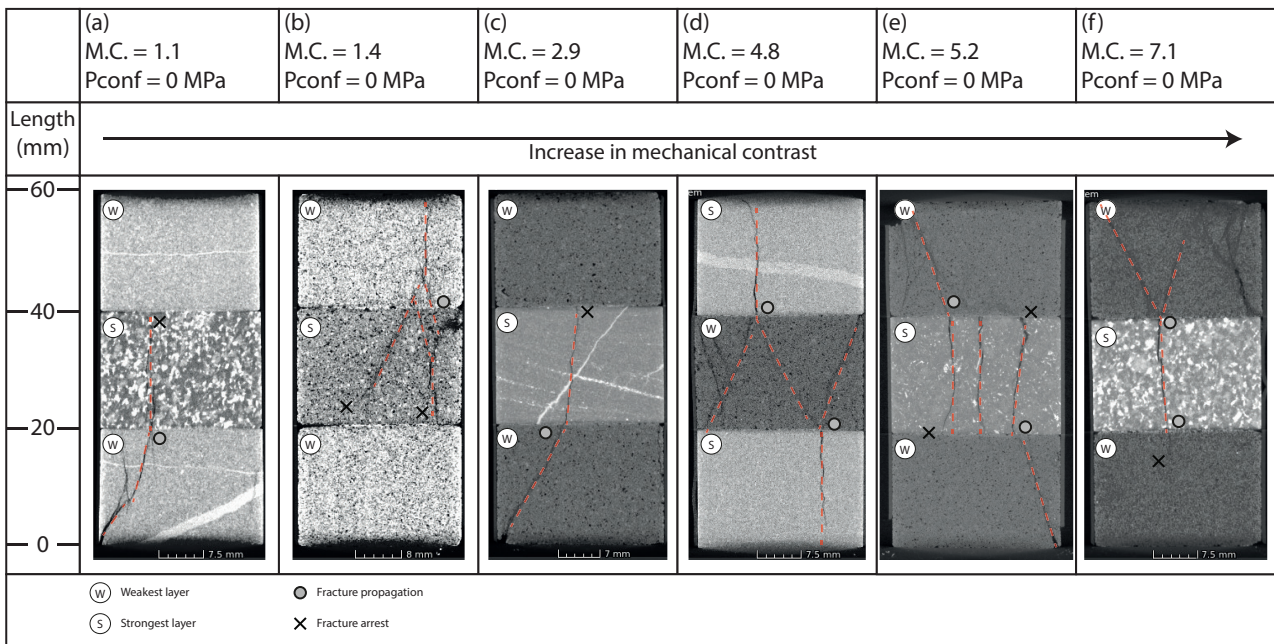


Figure 11: Micro-CT slices of performed experiments. Slices show fracture behaviour throughout several layered samples with different mechanical contrasts, at unconfined pressure conditions.

Figure 11(d) shows a micro-CT slices of a sample consisting of Ainsa sandstone and Bentheim sandstone, with Bentheim sandstone being the weakest rock in this combination, and Ainsa sandstone the strongest rock. The strength difference between these rocks results in a mechanical contrast of 4.8. Multiple shear fractures are created in the Bentheim sandstone layer in the middle of the sample, of which two propagate into the Ainsa sandstone layers at the top and bottom of the sample. The fractures extend all the way to the top and bottom ends of the sample.

Figure 11(e) shows a micro-CT slice of a sample consisting of Bentheim sandstone and Benin granite, with

Bentheim sandstone being the weakest rock in this combination, and Benin granite the strongest rock in this combination. The strength difference between these rocks results in a mechanical contrast of 5.2. Multiple shear fractures are created in the weaker Bentheim layers at the top and bottom of the sample, two of them propagate into the stronger granite layer in the middle, after which they are arrested at the next interface.

Figure 11(f) shows a micro-CT slice of a sample consisting of Red Felsler sandstone and Benin granite, with Red Felsler sandstone being the weakest constituent in this combination, and Benin granite the strongest. The strength difference between these rocks results in a mechanical contrast of 7.1. Multiple shear fractures are formed in the weaker Red Felsler layer at the top, of which one of them propagates into the granite layer in the middle of the sample. The fracture is arrested at the other interface.

In cases (a), (b), (c), (e) and (f), where the strongest layer is in the middle of the sample, fractures are arrested at the other interface after propagating through the middle layer. In case (d), the weakest layer is in the middle of the sample, and fractures propagate through the stronger layers at both sides. Shear fractures propagate through the interfaces into the stronger layers for all test setups with mechanical contrasts up to 7.1, at unconfined pressure conditions.

Several triaxial tests were performed on layered samples with mechanical contrasts ranging from 1.1 – 7.1, at confining pressures ranging from 10 MPa to 50 MPa. Samples were deformed under different confining pressure conditions, to investigate the influence of a confining pressure on the fracture patterns, and to validate if the results obtained at unconfined conditions still hold at confined pressure conditions.

Figure 12 shows the fracture behaviour for increasing confining pressure throughout samples consisting of Ainsa sandstone at the top and bottom and Benin granite in the middle of the samples. Ainsa sandstone is the weakest rock in this combination, Benin granite the strongest. The strength difference between these rocks results in a mechanical contrast of 1.1.

Multiple shear fractures were formed in the weakest layer at unconfined pressure conditions, Figure 12(a), and at confined (15 – 40 MPa) pressure conditions, Figures 12(b), (c) and (d).

At unconfined pressure conditions, a shear fracture propagates from the weaker layer into the stronger granite layer in the middle of the sample. The fracture is arrested at the other interface, Figure 12(a).

At a confining pressure of 15 MPa, multiple shear fractures exist in the sample which propagate through interfaces. There exists one large shear fracture that extends all the way through the sample, Figure 12(b).

At a confining pressure of 40 MPa, multiple shear fractures are initiated in the weakest layer at the top which propagate into the stronger granite layer in the middle. The fractures merge into one fracture in the granite layer, and the fracture is arrested at the other interface.

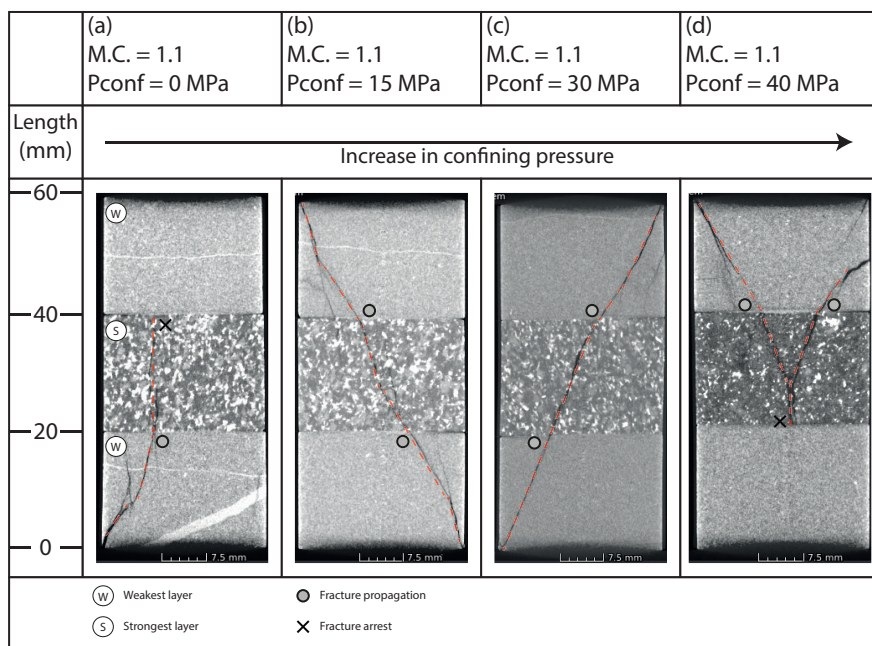


Figure 12: Micro-CT slices of performed experiments. The slices show fracture behaviour throughout samples consisting of Ainsa sandstone, Benin granite and Ainsa sandstone, for increasing confining pressure.

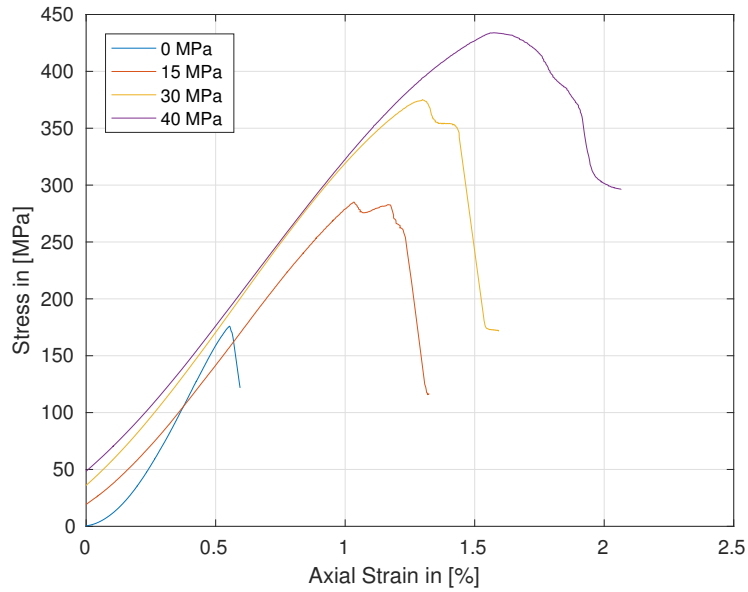


Figure 13: Stress-strain curves of tests on layered samples with a mechanical contrast of 1.1. The curves represent tests performed at different confining pressures.

The large connected shear fractures that extend all the way from the bottom to the top which are present in figures 12(b) and (c), are either formed by propagation of one shear fracture from one side to the other, or by merging of two independent shear fractures formed on both sides of the sample.

The test at unconfined pressure conditions was halted quickly after failure, see Figure 13. Fracture arrest at the upper layer interface in Figure 12(a) may be explained by the short period of loading after failure. Fracture arrest at the bottom layer interface in Figure 12(d) may be explained by the relatively high amount of strain after failure, shown in Figure 13. Stresses might be dissipated by the large amount of deformation in the top layer, rather than driving fracture propagation.

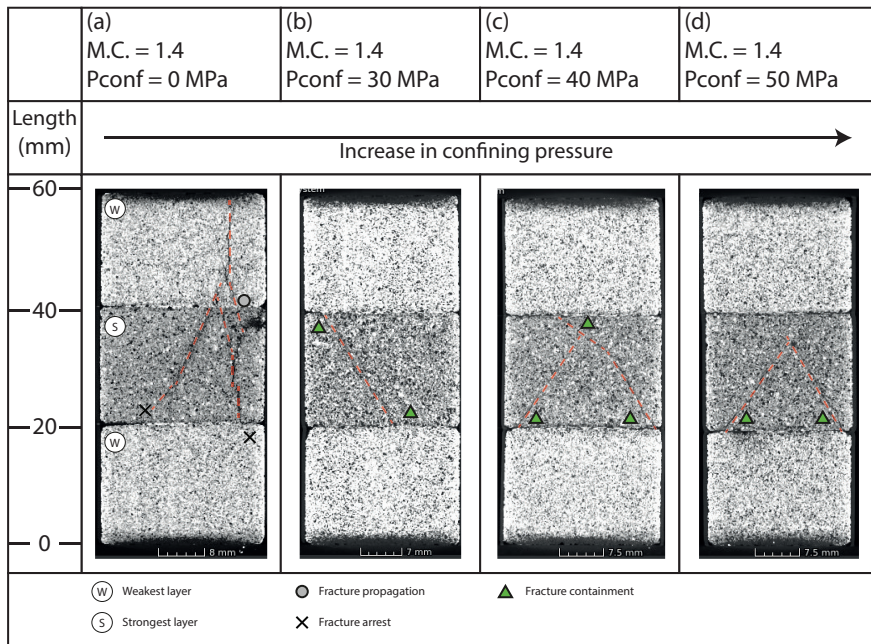


Figure 14: Micro-CT slices of performed experiments. The slices show fracture behaviour throughout samples consisting of Red Felser sandstone, Bentheim sandstone and Red Felser sandstone, for increasing confining pressure.

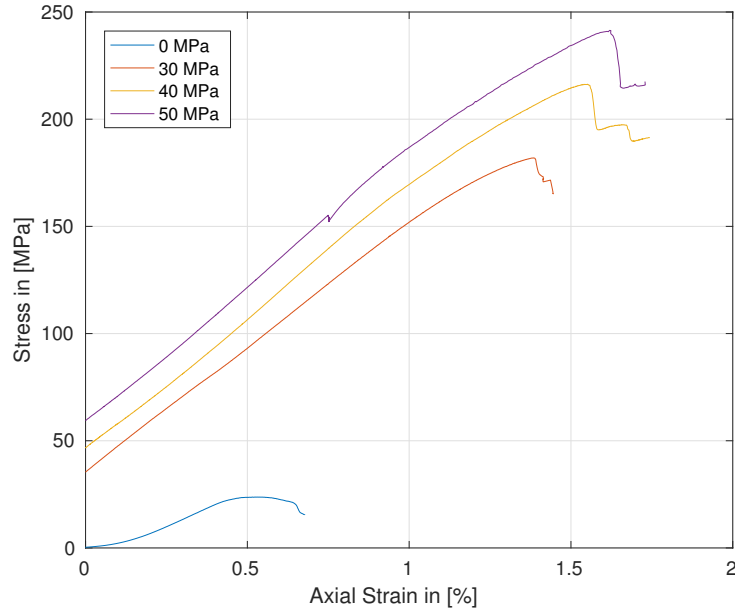


Figure 15: Stress-strain curves of tests on layered samples with a mechanical contrast of 1.4. The curves represent tests performed at different confining pressures.

Figure 14 shows the fracture behaviour for increasing confining pressure throughout samples consisting of Red Felser sandstone at the top and bottom and Bentheim sandstone in the middle of the samples. Red Felser sandstone is the weakest rock in this combination, Bentheim sandstone the strongest. The strength difference between these rocks results in a mechanical contrast of 1.4.

Multiple shear fractures were formed in the middle Bentheim sandstone layer, and in the Red Felser sandstone layer at the top, fractures propagate through the interface at the top, while fractures are arrested at the bottom interface. Two fractures merge into one in the top Red Felser layer. Figure 14(a).

At confining pressures from 30 – 50 MPa, fractures are contained in the middle Bentheim sandstone layer, Figures 14(b), (c) and (d). Stress-strain curves for the different tests are shown in Figure 15. Confined tests were all stopped when the stress after failure stabilized. No onset of fracture propagation was observed in the samples, which complies with the stress-strain data.

Figure 16 shows the fracture behaviour for increasing confining pressure throughout samples consisting of Bentheim sandstone at the top and bottom, and Beringen sandstone in the middle of the samples. Bentheim sandstone is the weakest rock in this combination, and Beringen sandstone the strongest rock. The strength difference between these rocks results in a mechanical contrast of 2.9.

At unconfined conditions, a single shear fracture is initiated in the weakest layer, and it propagates through the interface into the stronger Beringen sandstone layer in the middle of the sample. The fracture is arrested in the Beringen sandstone layer at the other interface, Figure 16(a).

At a confining pressure of 10 MPa, multiple shear fractures are initiated in the weaker Bentheim sandstone layer in the bottom, and one shear fracture propagates through the interface into the stronger Beringen sandstone layer in the middle. The fracture is arrested in the Beringen sandstone layer, Figure 16(b).

At confining pressures 20 – 40 MPa, shear fractures are contained in the layer in which they are initiated, Figures 16(c), (d) and (e).

The stress-strain data of all the experiments on samples with a mechanical contrast of 2.9 are shown in Figure 17. At unconfined pressure conditions, the fracture propagates until the top layer interface. Inhibition of fracture propagation may be explained by the quick halt of deformation after failure of the sample. Tests at confined pressure conditions were all stopped when the pressure after failure stabilized. At a confining pressure of 40 MPa, the stress-strain curve shows a sort of 'staircase' behaviour. These steps may coincide with the different fractures formed in the top layer of the sample shown in Figure 16(e).

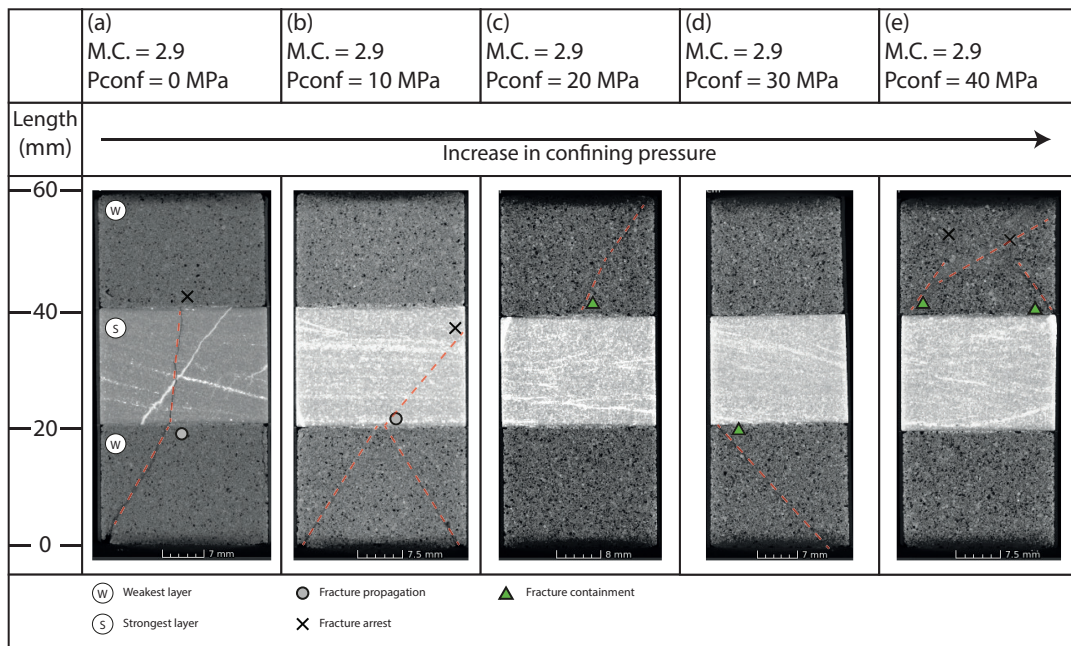


Figure 16: Micro-CT slices of performed experiments. The slices show fracture behaviour throughout samples consisting of Bentheim sandstone, Beringen sandstone and Bentheim sandstone, for increasing confining pressure.

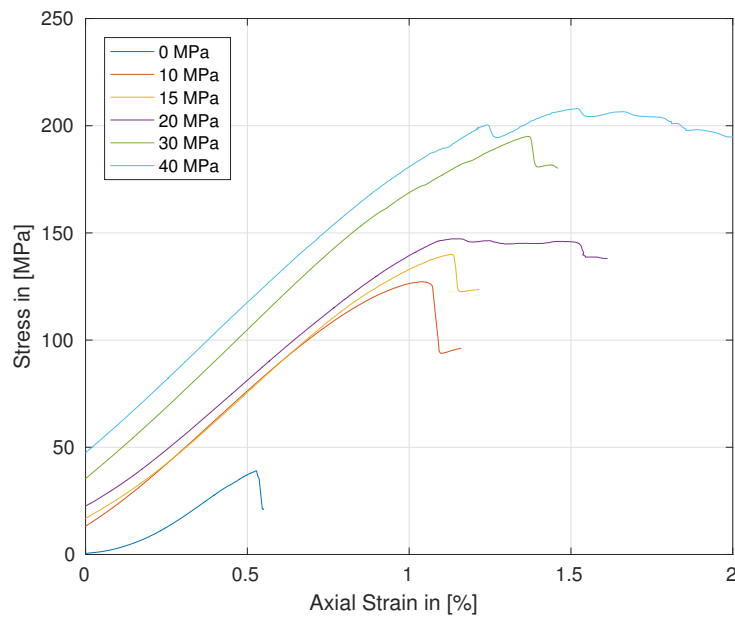


Figure 17: Stress-strain curves of tests on layered samples with a mechanical contrast of 2.9. The curves represent tests performed at different confining pressures.

Figure 18 shows the fracture behaviour for increasing confining pressure throughout samples consisting of Ainsa sandstone at the top and bottom of the samples, and Bentheim sandstone in the middle of the samples. Bentheim sandstone is the weakest rock in this combination, and Ainsa sandstone the strongest rock. The strength difference between these rocks results in a mechanical contrast of 4.8.

Multiple shear fractures were formed in the weakest rock layer and propagate through the interface into the more competent Ainsa sandstone at unconfined pressure conditions, Figure 18(a), and at confined pressure conditions up to 15MPa, Figures 18(b), (c). At confining pressures of 10 – 15 MPa, fracture arrest in the stronger Ainsa sandstone layer is observed, and the fracture thins out towards the other interface, Figures 18(b), (c). At confining pressures of 30 – 50 MPa, fractures are contained within the layer in which they were formed, Figures 18(d), (e), (f).

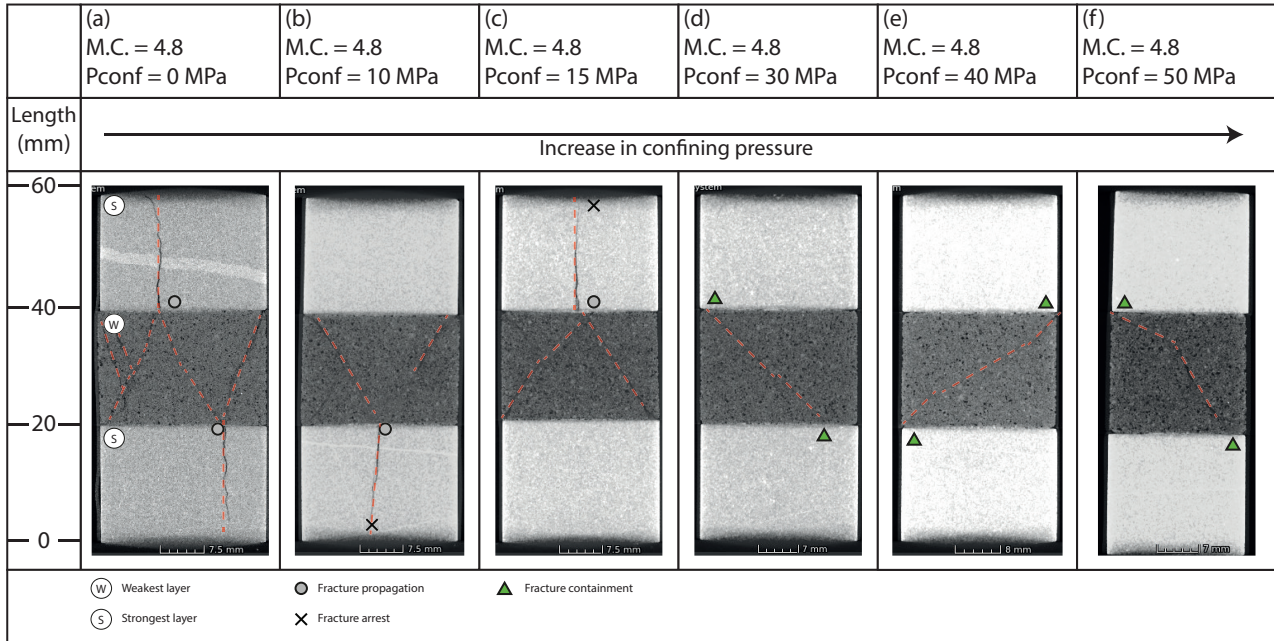


Figure 18: Micro-CT slices of performed experiments. The slices show fracture behaviour throughout samples consisting of Ainsa sandstone, Bentheim sandstone and Ainsa sandstone, for increasing confining pressure.

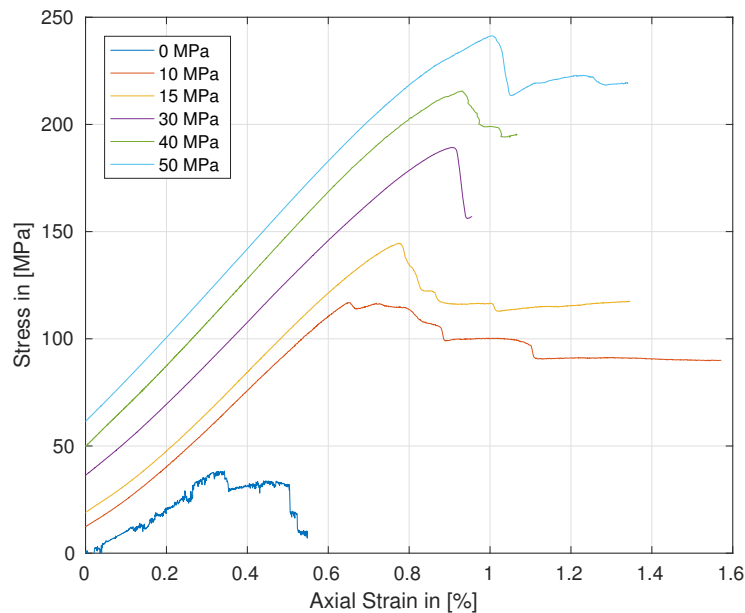


Figure 19: Stress-strain curves of tests on layered samples with a mechanical contrast of 4.8. The curves represent tests performed at different confining pressures.

The stress-strain data of all experiments on layered samples with a mechanical contrast of 4.8 are shown in Figure 19. The curve for unconfined pressure condition is very 'wiggly', the electrical signal from the machine was not filtered properly. Staircase behaviour in the stress-strain data at confining pressures of 10 and 15 MPa

might have caused conjugate fracture sets to be formed. Although deformation after failure was continued for the test at a confining pressure of 50 MPa, this did not result in any extra fractures to be formed in the weaker material.

Figure 20 shows the fracture behaviour for increasing confining pressure throughout samples consisting of Bentheim sandstone at the top and bottom of the samples, and Benin granite as the middle layer. Bentheim sandstone is the weakest rock in this combination, and Benin granite the strongest rock. The strength difference between these rocks results in a mechanical contrast of 5.1.

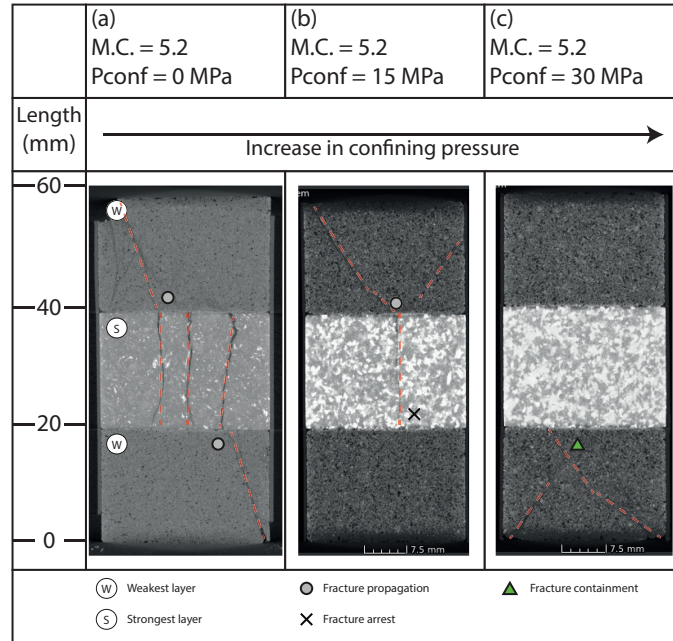


Figure 20: Micro-CT slices of performed experiments. The slices show fracture behaviour throughout Bentheim sandstone, Benin granite and Bentheim sandstone, for increasing confining pressure. Sample (a) courtesy of [Janmahomed \(2016\)](#).

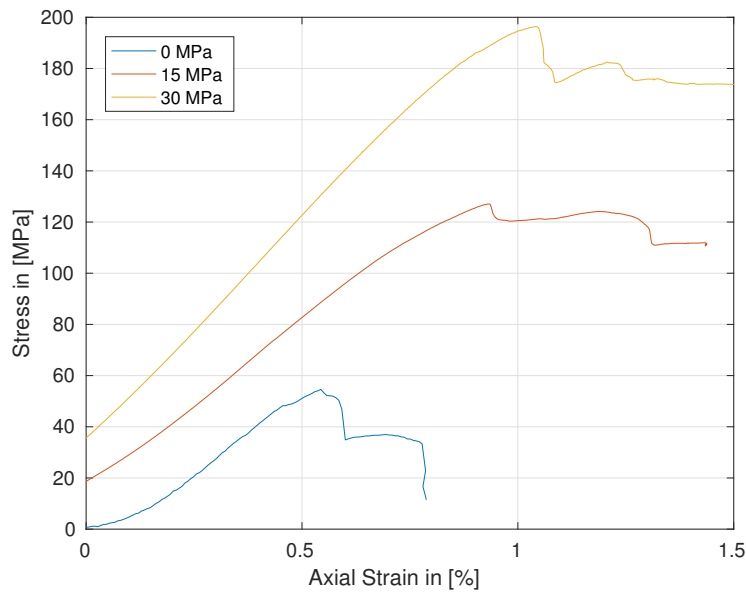


Figure 21: Stress-strain curves of tests on layered samples with a mechanical contrast of 5.2. The curves represent tests performed at different confining pressures. Data of unconfined test courtesy of [Janmahomed \(2016\)](#).

Multiple shear fractures were created in the weaker Bentheim sandstone layers at the top and bottom of the sample at unconfined conditions. Two shear fractures propagate through the interface into the stronger granite layer in the middle, after which they are arrested at the next interface, Figure 20(a).

At a confining pressure of 15 MPa, multiple fractures were initiated in the weaker Bentheim sandstone layer at the top, two shear fractures merge at the rock interface, and one fracture propagates through the interface into the granite layer in the middle, Figure 20(b).

At a confining pressure of 30 MPa, multiple shear fractures were formed, but were contained in the weaker Bentheim sandstone layer, Figure 20(c).

Stress-strain data of the tests performed on layered samples with a mechanical contrast of 5.2 are shown in Figure 21. Staircase behaviour is observed for every test, and may coincide with the formation of conjugate fracture sets.

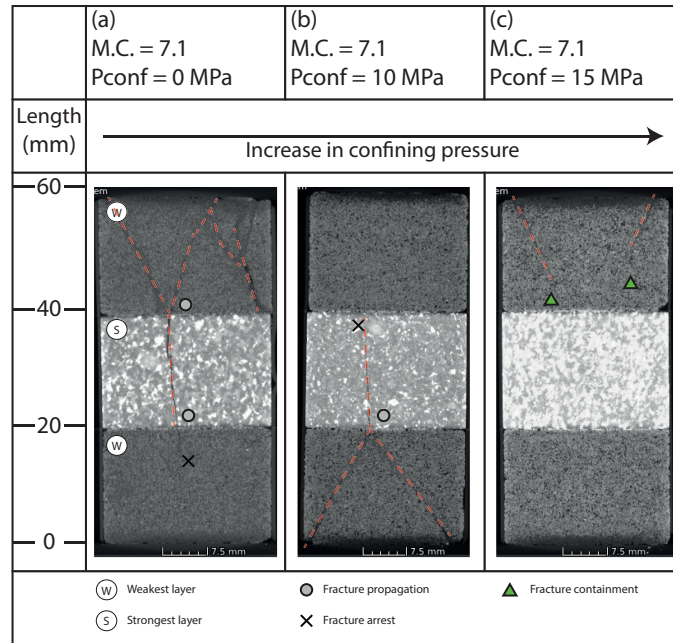


Figure 22: Micro-CT slices of performed experiments. The slices show fracture behaviour throughout Red Felser sandstone, Benin Granite and Red Felser sandstone, for increasing confining pressure.

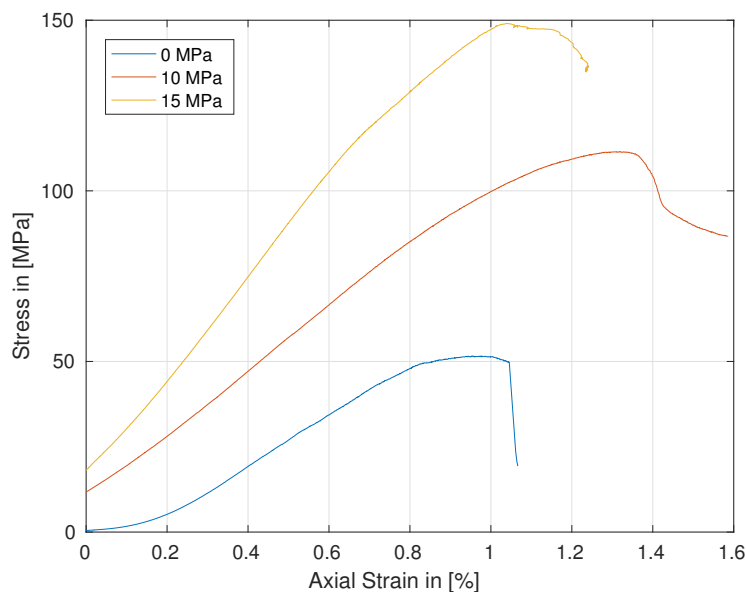


Figure 23: Stress-strain curves of tests on layered samples with a mechanical contrast of 7.1. The curves represent tests performed at different confining pressures.

Figure 22 shows the fracture behaviour for increasing confining pressure throughout samples consisting of Red Felser sandstone at the top and bottom of the samples, and Benin granite in the middle of the samples. Red Felser sandstone is the weakest rock in this combination, and Benin granite the strongest rock. The strength difference between these rocks results in a mechanical contrast of 7.1.

Multiple shear fractures were formed in the weaker layer at the top of the sample, at unconfined conditions. One fracture propagates through the upper interface, into the stronger layer in the middle, and also propagates through the lower interface into the weaker sandstone layer at the bottom. Other fractures were contained in the upper Red Felser sandstone layer, Figure 22(a).

At a confining pressure of 10 MPa, multiple shear fractures were created in the bottom Red Felser sandstone layer. One fracture propagates through the lower interface, into the granite layer in the middle. The fracture is arrested at the other rock interface, Figure 22(b).

At a confining pressure of 15 MPa, fractures were contained in the upper Red Felser sandstone layer, Figure 22(c).

Figure 23 shows the stress-strain data of tests performed on layered samples with a mechanical contrast of 7.1. All three curves show termination of loading relatively quickly after failure of the sample. No staircase behaviour in the stress-strain data is observed, however conjugate sets of fractures are observed in the micro-CT data. Staircase behaviour of stress-strain data does not necessarily have to coincide with the formation of fracture sets.

Figure 24 shows the fracture behaviour in sample consisting of Ainsa sandstone at the top and bottom of the sample, and Huesca siltstone in the middle. Huesca siltstone is the weakest rock in this combination, and Ainsa sandstone is the strongest rock. The strength difference between these rocks results in a mechanical contrast of 15.8. The test has been performed unconfined.

Multiple shear fractures are formed and contained in the weakest layer, Figure 24. The stress-strain data is shown in Figure 25. The data suggests that the onset of failure already started around 9 MPa.

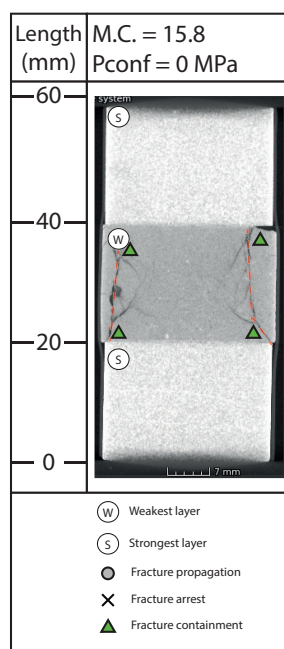


Figure 24: Micro-CT slice of fracture behaviour throughout a sample consisting of Ainsa sandstone, Huesca siltstone and Ainsa sandstone with no confining pressure.

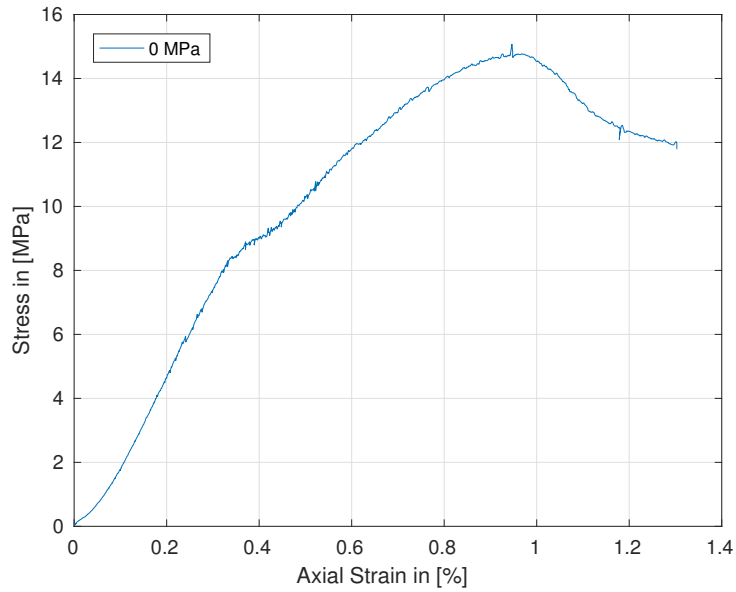


Figure 25: Stress-strain curve of test on layered sample with a mechanical contrast of 15.8. The curve shows data of a test performed at unconfined pressure.

A summary of all test results is presented in figure 26. It provides an overview of whether fractures were contained within the weakest layers, or whether fractures propagate through layer interfaces. Figure 26 also shows the influence of mechanical contrast and confining pressure on stress-induced fracturing in synthetically layered rock samples. A gradual downward trend of confining pressure for increasing mechanical contrast is observed. It seems that lower compressive horizontal stresses are needed in order to contain fractures within the weakest layer when the mechanical contrast increases.

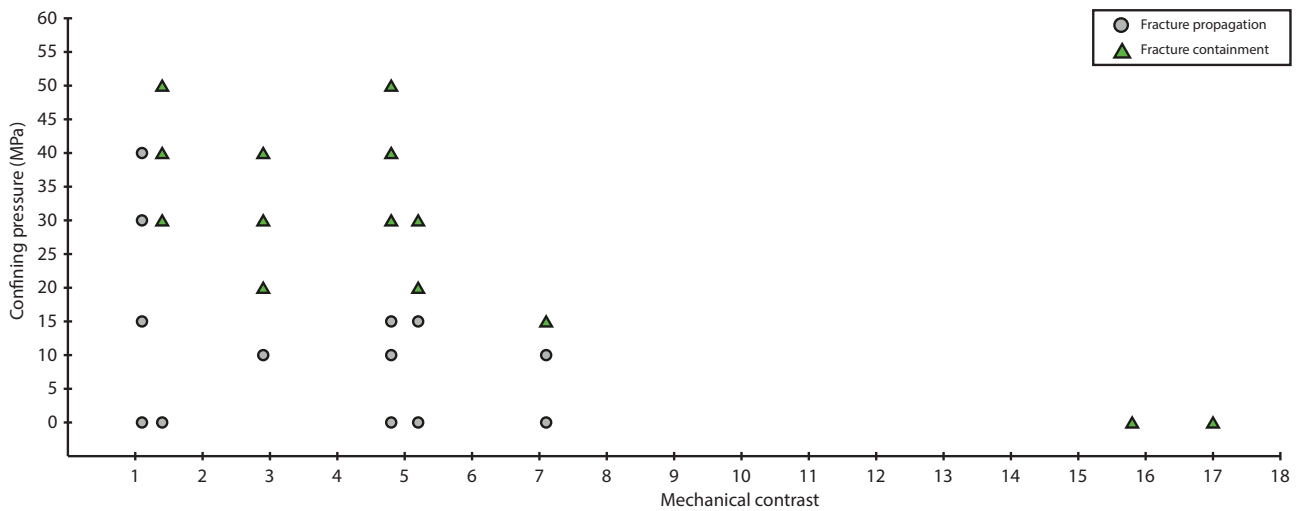


Figure 26: Summary of all test results on fracture containment/propagation in layered samples. Fracture propagation and fracture containment is shown for tests at different mechanical contrasts and confining pressures.

3.3 Fracture aperture

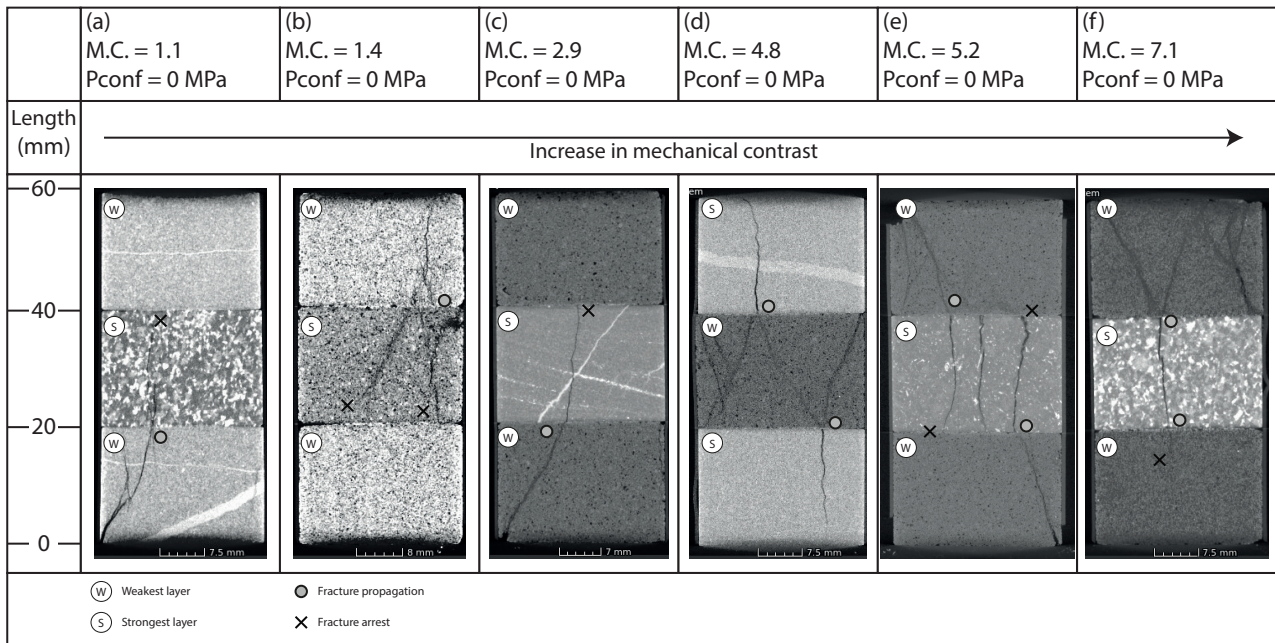


Figure 27: Micro-CT slices of layered samples with various mechanical contrasts (M.C.) at unconfined pressure conditions.

Analysis of micro-CT data showed that changes in fracture aperture occur along the fracture pathway. The displayed images are 2D slices, although changes in fracture aperture were observed in 3D as well.

Figure 27 shows micro-CT slices of samples with different mechanical contrasts at unconfined pressure conditions. Several samples show the same behaviour, the fracture aperture decreases when the fracture propagates from the bottom layer to the middle layer, and it tapers away towards the layer interface between the middle and top layer in Figures 27(a,c). Figure 27(d) shows the same behaviour, only in this case the fractures propagate from the middle layer to the outer layers. The fracture apertures gradually thin out towards the top and bottom of the sample.

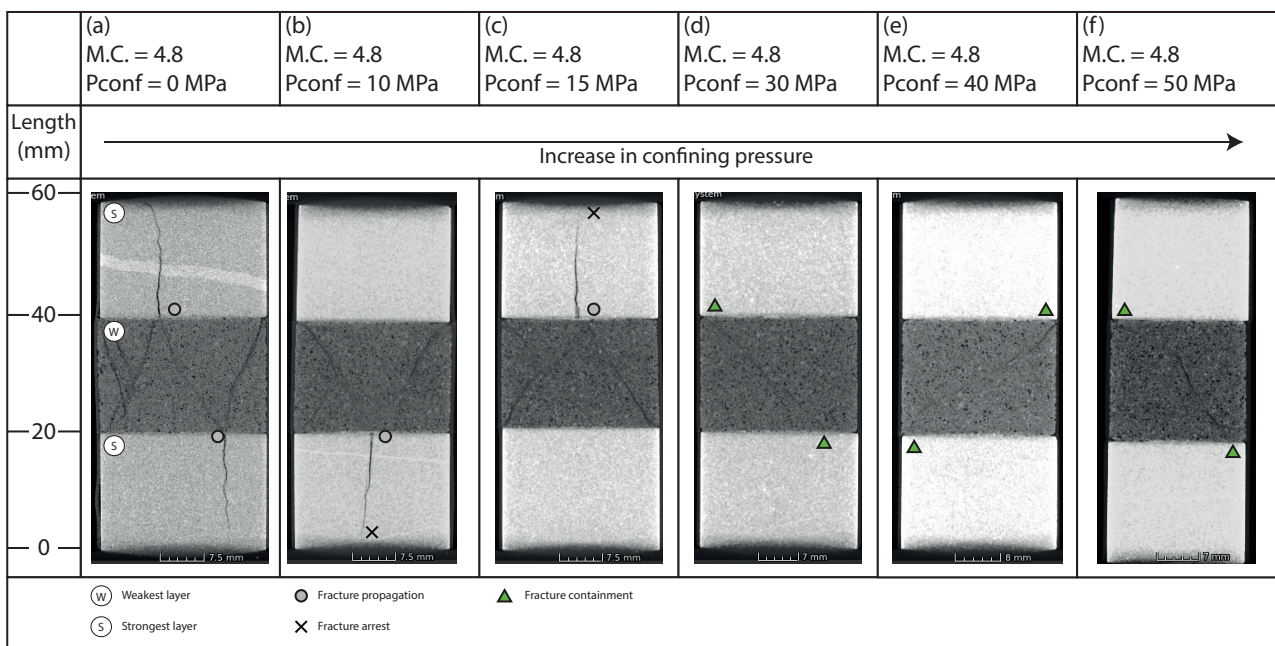


Figure 28: Micro-CT slices of layered samples with a mechanical contrast of 4.8, at different confining pressures.

The fracture aperture also changes when the fracture propagates from the top layer into the middle layer in Figure 27(f), the fracture aperture gradually decreases. For Figures 27(b,e) there does not appear to be a significant change in fracture aperture. Changes in fracture aperture in Figures 27(b,f) are not so apparent as a damaged zone is present around the fractures.

In most cases slight changes in fracture aperture for fractures propagating through multiple layers are observed. Changes in fracture aperture are similar for samples with various mechanical contrasts, there does not appear to be a trend in change in fracture aperture with increasing mechanical contrast.

Figure 28 shows a sequence of triaxial tests run on the same sample configuration, for increasing confining pressure. The samples consist of Ainsa sandstone as the top and bottom layers, and Bentheim sandstone as the middle layer. This sample configuration was chosen to highlight the effect of confining pressure. Micro-CT images of other sample configurations are shown in the previous section.

Figure 28 shows that the fractures exhibit the same behaviour in the Ainsa sandstone layers. The fracture aperture gradually decreases towards top or bottom of the sample. Changes in fracture aperture along the pathway of fractures that propagate through multiple layers are not so apparent. Fracture aperture in the middle layer of the samples gradually decreases for increasing confining pressure. Confining pressure appears to have an influence on fracture aperture.

3.4 Fracture orientation

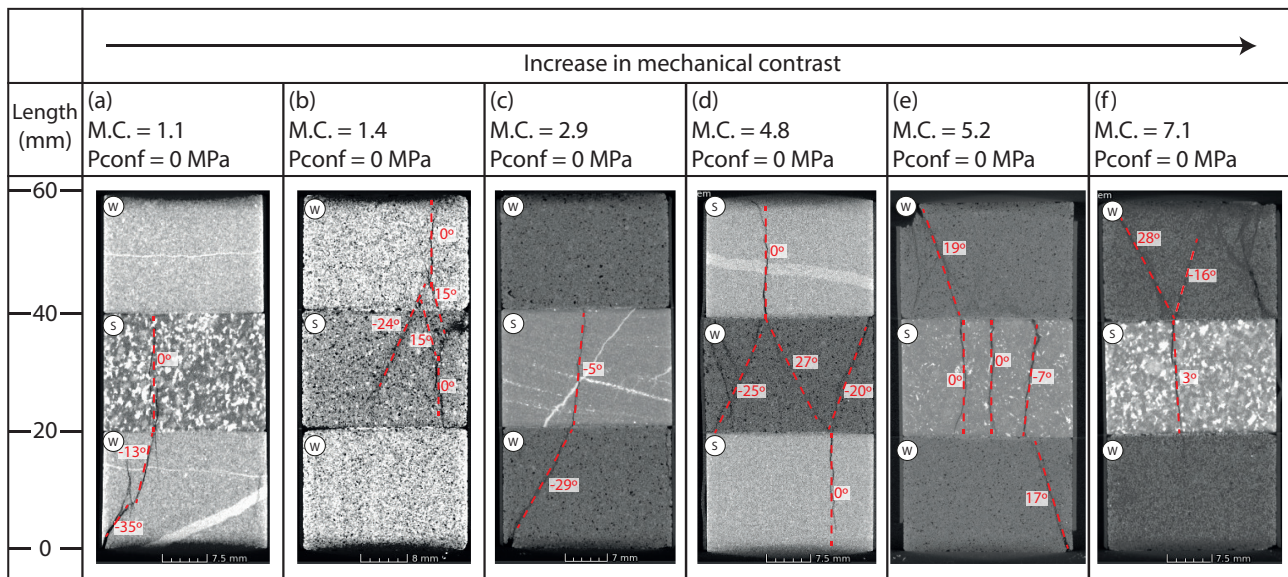


Figure 29: Micro-CT slices of layered samples with varying mechanical contrasts at unconfined pressure conditions.

Analysis of micro-CT images showed that changes in fracture orientation occur along the fracture pathway, and that refraction of fractures occurs at layer interfaces. A subset of images is shown in this section, a full list of images is shown in Appendix B, page 55.

Figure 29 shows a series of micro-CT slices of layered samples with different mechanical contrasts, at unconfined pressure conditions. A description of the samples, and of which lithologies they consist can be found in section 3.2 on page 26.

At unconfined pressure conditions, the samples in Figure 29 all show roughly the same behaviour. Refraction of fractures at the layer boundaries is observed in Figures 29(a-f). The orientation of the fracture changes towards (near-) vertical in the stronger material.

In the samples with a mechanical contrast of 1.1 and 1.4, changes in fracture orientation in the same material were observed, Figures 29(a,b). For samples with mechanical contrasts in the range from 2.9 - 7.1 no changes in fracture orientation in the same material were observed, see Figures 29(c-f).

Fractures refract at the layer interface in samples with mechanical contrasts of 1.1 - 7.1 at unconfined pressure conditions. Fractures propagate (near-) vertically in the stronger layer after refraction.

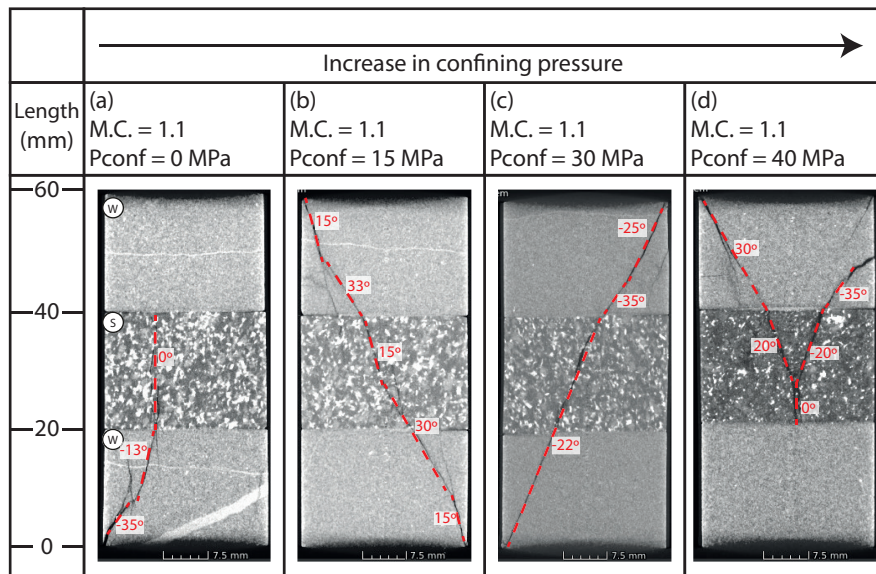


Figure 30: Micro-CT slices of layered samples with a mechanical contrast of 1.1, for increasing confining pressure.

Figure 30 shows a series of micro-CT slices of layered samples with the same mechanical contrast, for increasing confining pressure. The samples consist of Ainsa sandstone as the top and bottom layer, and Benin granite as the middle layer.

Figure 30(a) shows a slight refraction of the fracture at the interface between the bottom and middle layer. The fracture slightly changes dip in the bottom layer. Figure 30(b) shows a single shear fracture which propagates throughout the sample. There is some refraction at the interface between the top and middle layer, but the overall orientation is roughly the same. Figure 30(c) also shows a single shear fracture throughout the sample, there is some refraction of the fracture at the interface between the top and middle layer. Figure 30(d) shows two fractures in the top layer that merge in the middle layer. Both fractures show some refraction at the interface between the top and middle layer. Refraction also occurs when the fractures merge in the middle layer.

Figure 31 shows a series of micro-CT slices of layered samples with the same mechanical contrast, at increasing confining pressure. The samples consist of Ainsa sandstone as the top and bottom layer, and Bentheim sandstone as the middle layer.

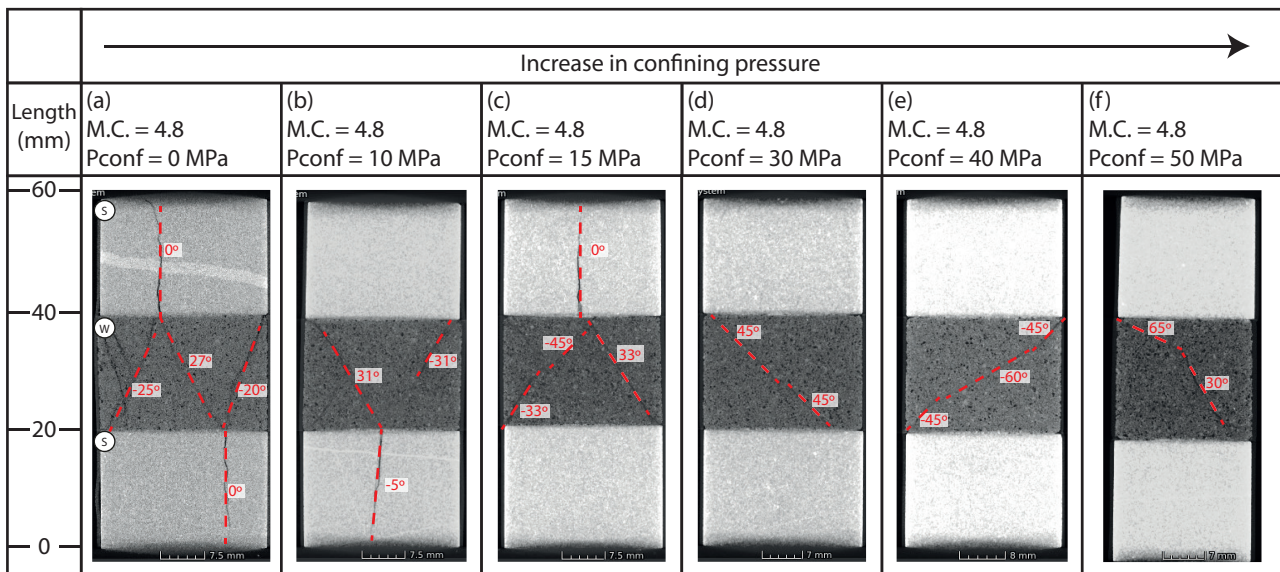


Figure 31: Micro-CT slices of layered samples with a mechanical contrast of 4.8, for increasing confining pressure.

Figure 31(a) shows conjugate fracture sets in the middle layer, refraction occurs at both interfaces, and fracture orientation in the top and bottom layers is vertical. Figure 31(b) shows a conjugate fracture set in the middle layer, and refraction of a fracture at the interface between the middle and bottom layer. Fracture orientation is almost vertical in the bottom layer. Figure 31(c) also shows a conjugate fracture set in the middle layer, and refraction of a fracture at the interface between the top and middle layer. Fracture orientation in the top layer is vertical. Figures 31(d,e,f) show shear fractures in the middle layer, fracture dip changes along the fracture pathway.

Experimental results show that at low mechanical contrasts, refraction of the fracture is less likely to occur. The shear fracture that is formed in the weaker layer, propagates into the stronger layer and maintains its orientation. At higher mechanical contrasts, results shows that refraction of fractures almost always occurs, fracture orientation changes to (near-) vertical in the stronger layers.

Refraction of fractures is influenced by mechanical contrast, confining pressure doesn't seem to influence the change in fracture orientation at the layer interface.

3.5 Fracture mode

Refraction of fractures at layer interfaces are observed in many micro-CT scans of layered samples. Changes of fracture orientation at the layer interface commonly coincide with a change in fracture mode. Figure 32 shows a vertical and horizontal slice of a conjugate set of fractures in a layered sample consisting of Ainsa sandstone as the top and bottom layer and Bentheim sandstone as the middle layer. The horizontal slice in Figure 32(b) shows a cross-section of the fractures. Both pictures indicate that shear fractures were formed in the middle layer, dilation of the fracture is minimal, and there appears to be a damaged zone rather than a clear fracture. The same fracture is traced into the top layer, micro-CT slices are shown in Figure 33. The horizontal slice in Figure 33(b) shows a cross-section of the fracture. Both pictures indicate that an opening fracture was formed in the top layer, dilation of the fracture is clearly visible, and there is no damaged zone around the fracture.

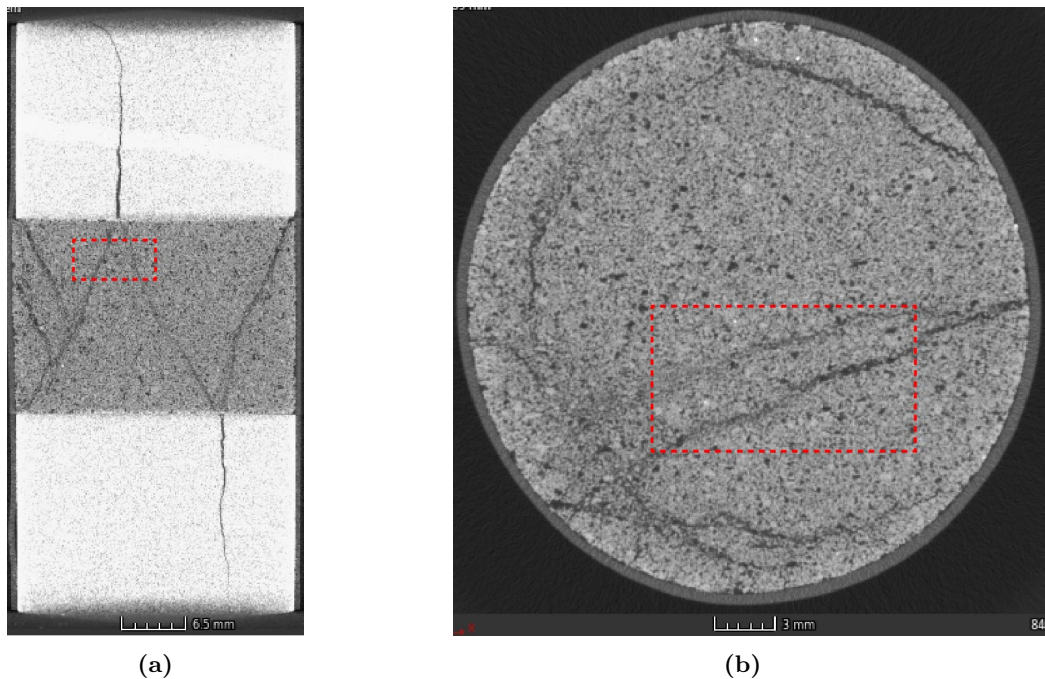


Figure 32: (a) Vertical micro-CT slice of a layered sample. (b) Horizontal micro-CT slice of a layered sample. The highlighted sections correspond with each other.

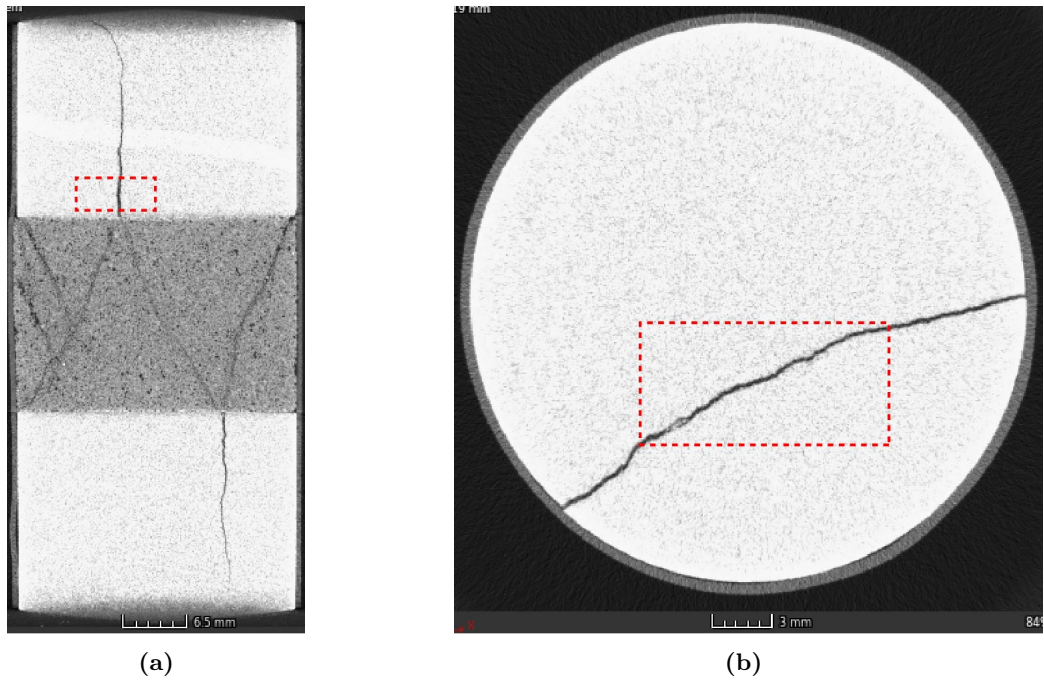


Figure 33: (a) Vertical micro-CT slice of a layered sample. (b) Horizontal micro-CT slice of a layered sample. The highlighted sections correspond with each other.

3.6 Fracture step-over

2D images of 3D fractures in samples showed signs of step-over at layer interfaces for fracture propagation. These fractures have been traced and an example is shown in Figure 34.

The 2D representation of a 3D sample does not always lead to correct interpretations as is shown. On the left, the fracture tips in the materials on both sides of the interface are horizontally separated, leading to the interpretation that fractures step-over at layer interfaces. However, when this fracture was traced throughout the sample (further to the right) the horizontal distance between the fracture tips decreased, and fracture tips align.

In this case, horizontal distance between the fracture tips is also caused by the existence of a conjugate set of fractures in the middle layer. The fracture in the top layer aligns with one of the fractures in the middle layer, creating an apparent step-over fracture.

Cooke and Underwood (2001) state that step-over fractures in homogeneous rocks are not observed in the field. They suggest that deformation along the layer interface must alter the stress field in such a way that step-over fractures develop rather than planar propagation.

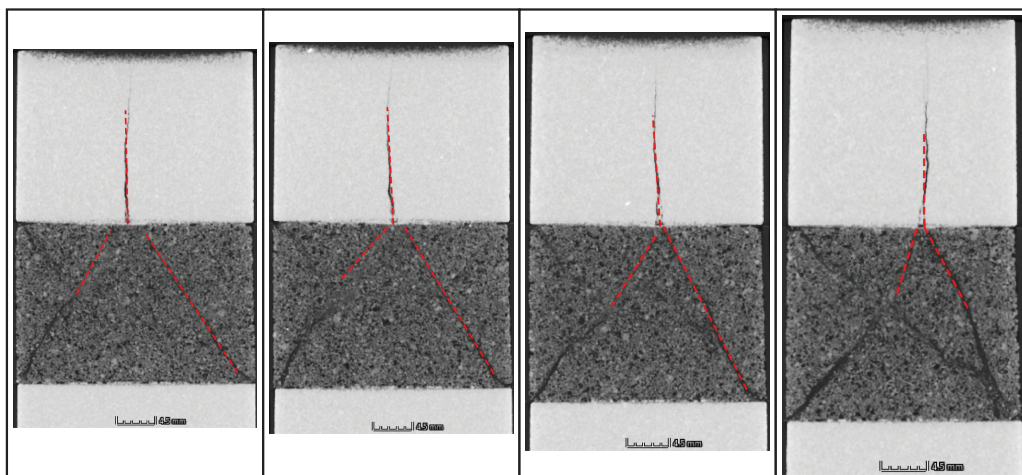


Figure 34: Images show apparent fracture step-over throughout the sample.

Chapter 4

Discussion

4.1 Initiation of fracture in weakest layer

For a layered sample, it has been shown that fracture initiation is likely to occur in the weakest layer, irrespective of mechanical contrast. The ultimate strength of the layered sample is much closer to that of the weakest layer, compared to the strength of the strongest layer. With strength differences between the composite sample and the weakest layer ranging from 8% to 65%, and strength differences between the composite sample and the strongest layer ranging from 328% to 542%.

The experimental results suggest that fractures initiate in the weakest layers, which also have the lowest Young's modulus. This is contrary to what is suggested by many authors, that fractures initiate in stiff layers and arrest at interfaces with soft layers (Brenner and Gudmundsson, 2004; Cooke et al., 2006; Morris et al., 2009; Ferrill et al., 2014, 2017). This difference in results may be explained by the difference in mechanical stratigraphy. Experiments have been performed on lithologies which all deform brittle. Brenner and Gudmundsson (2004); Cooke et al. (2006); Morris et al. (2009); Ferrill et al. (2014, 2017) all mention soft layers which contain major amounts of clay, and which deform ductile. While stiffness might be a valid measure for the studies presented by Brenner and Gudmundsson (2004); Cooke et al. (2006); Morris et al. (2009); Ferrill et al. (2014, 2017), it does not fully cover fracture initiation and needs to be coupled with the deformation style. The rock mechanical parameter strength is more indicative for fracture initiation.

4.2 Containment of fractures

Unconfined experiments have been performed on layered samples to investigate the fracture behaviour at these conditions. Results showed that for layered samples with mechanical contrasts ranging from 1.1 to 7.1, fractures propagated through the interfaces into the strong layer, see Figure 11. For layered samples with mechanical contrast of 15.8 and 17, fractures were contained within the weaker layer, see Figure 24.

The test samples consist of stacked layers of rock, which are separated by an interface. As there is no bonding of the different layers, the interface can be considered as a discontinuity. According to Gudmundsson and Brenner (2001), three combined factors contribute to fracture arrest, of which two are applicable to these results: discontinuities between layers and changes in stiffness between layers. Cooke et al. (2006); McGinnis et al. (2017) suggest low shear strength and poorly bonded interfaces help terminate fracture propagation. Low interfacial shear strength and poorly bonded interfaces correspond with abrupt lithological and mineralogical transitions between layers (McGinnis et al., 2017). Although the test settings conformed to the conditions of Gudmundsson and Brenner (2001); Cooke et al. (2006); McGinnis et al. (2017) for fracture arrest, samples with large changes in stiffness between layers (up to a contrast of 7.1), and poorly bonded interfaces all showed fracture propagation.

A reason for this might be that the stress-concentration at the fracture tip is higher than the tensile strength of the rock, and a new fracture is initiated. Cooke et al. (2006) found that adjacent layers may not be soft enough to resist fracture propagation because of the stress concentration at the fracture tip. In this case, soft refers to layers which deform ductile and are able to accommodate high amounts of strain before failure. Generally a new fracture initiates if the maximum tensile stress on the intact side of the interface exceeds the tensile strength of the material (Cooke and Underwood, 2001). Fractures may generate very high crack-tip tensile stresses, as much as four orders of magnitude greater than the in-situ tensile strength of the host rock (Gudmundsson and Brenner, 2001).

Fracture propagation was inhibited for layered samples with mechanical contrasts of 15.8 and 17, conforming to the conditions proposed by Gudmundsson and Brenner (2001); Cooke et al. (2006); McGinnis et al. (2017)

which suggest discontinuities between layers and changes in stiffness inhibit fracture propagation. The results from experiments on unconfined samples suggest that the interplay between strength of the rock and crack-tip tensile stress is an important control in fracture propagation at unconfined conditions.

Experimental results of triaxial tests on layered samples indicate that mechanical contrast and confining pressure influence fracture propagation in layered rock samples. Lower horizontal compressive stresses are needed in order to contain the fracture in the weakest layer when the mechanical contrast increases, see Figure 26.

For a fixed mechanical contrast, fractures are contained when confining pressure is increased, see Figure 18. It is generally known that for increasing confining pressure, $\sigma_2 = \sigma_3$, the rock strength increases due to the supporting stress (Michelis, 1985; Haimson and Chang, 2000). Fracture containment might be explained by the concept of stress barriers. When a layered rock mass is horizontally compressed, stiff layers would take up most of the compressive stress, and may become highly stressed, and act as barriers to fracture propagation (Gudmundsson and Brenner, 2001; Brenner and Gudmundsson, 2004). Stress barriers are layers with high fracture-normal compressive stresses that negatively impact fracture growth.

4.3 Prediction of fracture propagation in the subsurface

The experimental results on the control of mechanical contrast and confining pressure on fracture containment can be implemented by correlating confining pressure to burial depth, to predict fracture containment in the subsurface. Three different models describing changes in stress state through the crust are used to relate the confining pressure (σ_3) to burial depth. Differences in depth models reflect different assumptions on which the models are based.

Anderson (1951); Handin et al. (1963) suggest a theoretical model with isotropic stresses: $\sigma_1 = \sigma_2 = \sigma_3 = \rho gz$. Zoback (2007) suggests a theoretical model with the horizontal stress equal to 60% of the principal stress: $\sigma_3 = 0.6\sigma_1 = 0.6\rho gz$. Fossen (2010) suggests a theoretical model with the horizontal stress equal to one third of the principal stress: $\sigma_3 = 1/3\sigma_1 = 1/3\rho gz$.

The two principal horizontal stresses are equal ($\sigma_2 = \sigma_3$), and remain constant during the duration of the experiment. This experimental limitation does not necessarily correspond to the actual stress state of the subsurface (Handin et al., 1963).

Fracture containment in layered rocks in the subsurface can also be predicted by comparing confining pressures to the horizontal stresses in the subsurface. Magnitudes of horizontal stresses can be measured directly from the borehole (Vernik and Zoback, 1992). These measurements are more accurate than the depth values estimated by the different theoretical models. Usage of direct measurement of confining pressure is preferred to predict fracture containment in the subsurface based on the experimental results.

Figure 35 shows fracture behaviour for lithologies with varying mechanical contrasts at different confining pressures, and their correlated depths, according to one of the three models. Interpreted areas of fracture containment and fracture propagation are based on the experimental results. Figure 35 shows that fracture propagation into the stronger layer is favourable at shallow levels in the upper crust, whereas fracture containment is favourable at deeper levels. The range of realistic mechanical contrasts (1.1 - 5.2) indicates that fracture propagation is only expected to occur in the first few kilometers of the upper crust.

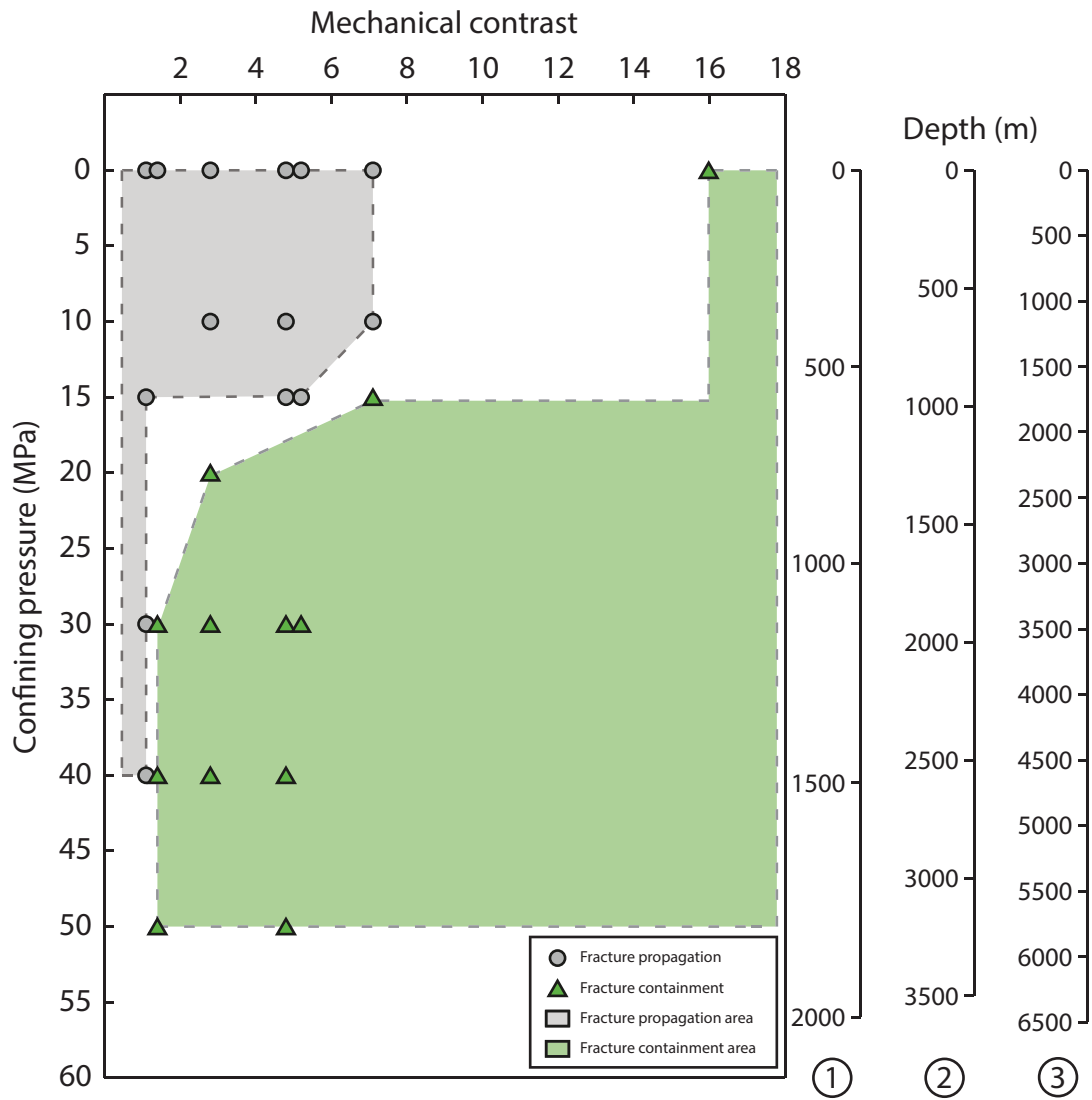


Figure 35: Overview of experimental results for varying mechanical contrast and confining pressure, correlated to depth. Depth correlations correspond to theoretical models of 1: (Anderson, 1951; Handin et al., 1963), 2: (Zoback, 2007), 3: (Fossen, 2010) .

4.4 Changes in fracture aperture

Experimental results indicated that mechanical contrast had no influence on fracture aperture at unconfined conditions. Experiments have been performed on layered samples with mechanical contrasts from 1.1 - 7.1. While there are slight changes in fracture apertures, a trend is not visible. Several experiments showed a smaller fracture aperture in stronger rocks, than in weaker rocks. This behaviour can be explained by a difference in Young's modulus. A higher Young's modulus means a larger resistance to deformation, and hence a smaller fracture aperture (Brenner and Gudmundsson, 2004; Gudmundsson, 2011).

The experimental results also indicated that confining pressure does have an influence on fracture aperture. With increasing confining pressure, fracture aperture of contained fractures decreases, see Figure 28. It is more difficult to dilate a fracture due to the supporting horizontal stress, and the rock strength increases due to the supporting horizontal stress (Michelis, 1985; Haimson and Chang, 2000). Brenner and Gudmundsson (2004) also suggest that remote loading influences aperture variation, stiff layers concentrate compressive stresses and fractures would open still less inside these layers.

Understanding the development of fractures can improve fluid flow prediction and benefit prediction of fracture characteristics (Underwood et al., 2003). Constraining uncertainty in fracture aperture therefore can aid permeability characterization, as fracture aperture is an intrinsic part of quantifying the effective permeability of fractures (Olson et al., 2009). Relating confining pressure to fracture aperture therefore can aid the quantification of effective permeability of fractures.

4.5 Changes in fracture orientation

Experimental results showed refraction of fractures in layered samples with mechanical contrasts ranging from 1.1 - 7.1 at unconfined pressure conditions. Fracture orientation changed to (near-) vertical in the stronger layer at the layer interface.

At confined pressure conditions, only a small amount of change in fracture orientation was observed, or no change at all in samples with low mechanical contrasts. Samples with higher mechanical contrasts (1.4 - 7.1) all clearly showed refraction of fractures at different confining pressures.

The experimental results indicated that refraction of fractures is influenced by the mechanical contrast of the layers. Confining pressure does not seem to have an influence on refraction.

Laboratory experiments showed that fractures commonly have variable orientations when they cut mechanically layered systems, which is in agreement with the findings of [Roche et al. \(2012\)](#); [Ferrill et al. \(2017\)](#) in field studies. Variation in fracture orientation may be explained by variations in the local effective stress state ([Ferrill and Morris, 2003](#); [Roche et al., 2012](#)), or can be related to variable mechanical properties of the layers they cut ([Ferrill and Morris, 2003](#); [Ferrill et al., 2017](#)).

Experiments on layered samples with low mechanical contrast showed only small, or no changes in fracture orientation. This may be explained by the fact that the layered sample acts as a relatively homogeneous mass because of small differences in rock mechanical parameters. [Ferrill et al. \(2017\)](#) suggest that in homogeneous strata fractures can be expected to fail with a consistent shear failure angle.

Experiments on layered samples with higher mechanical contrasts (1.4 - 7.1) showed refraction of fractures in all experiments. Refraction is a response to the different mechanical properties of different layers ([Ferrill and Morris, 2003](#); [Schöpfer et al., 2007](#); [Roche et al., 2012](#)). Fracture orientation changes from moderate dips in the weak layers to high dips in the stronger layers. [Ferrill and Morris \(2003\)](#); [Roche et al. \(2012\)](#) suggest this behaviour is closely linked to the fracturing mode, whereas steep sections are attributed to opening-mode fractures and moderately dipping sections to shear fractures, corresponding to the experimental results of this study.

Mechanical contrast between rock layers greatly influences fracture orientation, which in turn influences fracture architecture ([Ferrill et al., 2017](#)). Correctly interpreting fracture orientation benefits characterization of fracture architecture. Fracture architecture consists of, but is not limited to, fracture geometry, distribution and connectivity. It has been shown that for mechanical contrasts ranging from 1.4 - 7.1, fractures change orientation to (near-) vertical. These results in combination with the dilation tendency of opening-mode fractures ([Ferrill et al., 2017](#)) can benefit characterization of permeability architecture in subsurface reservoirs.

Chapter 5

Conclusion

This study investigates the control of mechanical contrast and confining pressure on fracture behaviour in layered rocks. Unconfined and confined compression tests were performed on three-layered samples with varying mechanical contrasts at different confining pressure conditions.

The results show that fractures initiate in the weakest layer, and propagate through the layer interface or are contained within the weakest layer.

Unconfined compressive strength tests showed that differences in rock strength do not always act as a containment barrier. Fractures propagated through the layer interface for mechanical contrasts up to 7.1.

The combination of mechanical contrast and confining pressure does control the containment of fractures within a layer. Lower horizontal compressive stresses are required to contain fractures when the mechanical contrast increases. Stronger layers have sufficiently high strength to inhibit fracture propagation. At higher confining pressures stronger layers may act as more effective stress barriers.

Mechanical contrast does not seem to influence fracture aperture. Confining pressure however greatly influences aperture as it limits the ability of fractures to dilate.

Results show that fracture orientation is controlled by mechanical contrast. Fractures refract at layer interfaces when the mechanical contrast is sufficiently high. At a low mechanical contrast (1.1) fracture orientation tends to be similar throughout the layers, at higher mechanical contrasts fracture orientation differs from layer to layer. Confining pressure does not seem to affect the refraction of fractures.

These results can improve the understanding of fracture containment, fracture aperture and fracture orientation in layered rocks at subsurface conditions. The mechanical contrast of the layered rocks, combined with the stress conditions need to be considered when characterizing subsurface fracture networks. Vertical connectivity between layers is of importance when predicting fluid flow through reservoirs. As fractures often serve as preferential fluid flow paths, correctly interpreting fracture characteristics is important for successful development of layered reservoirs.

Chapter 6

Recommendations

Mechanical stratigraphy consists of the interplay between rock strength and layer thickness (Morris et al., 2009). Since natural fractures are subject to controls imposed by mechanical stratigraphy, focusing on the mechanisms that control natural fracture development can improve fracture characterizations (McGinnis et al., 2017). In order to examine the control of mechanical stratigraphy on fracture behaviour more thoroughly, this study can be extended to examine the influence of layer thickness as well. Layer thickness is of particular importance on fracture containment as thin layers of strong rock will be breached more easily than thicker layers of the same material (Morris et al., 2009).

According to Gudmundsson and Brenner (2001), discontinuities at contacts between rock layers with different mechanical properties are also of importance in fracture arrest. The term discontinuity is used here for any mechanical break that affects the stress field.

In three-layered experiments, samples consist of three layers of rock stacked on top of each other. The interface between the different layers is unbonded, in which there is a lack of tensile strength. Shear stress can be transmitted across the interface, but depends on the cohesion and frictional properties of the interface (Teufel and Clark, 1984). Fracture propagation was observed in experiments on samples with various mechanical contrasts and at different pressure conditions. However, the experimental results could be improved by incorporating the effect of the layer interface on fracture behaviour.

Changes in fracture aperture were observed visually, and the fracture aperture was not thoroughly measured throughout the sample. Examination of fracture aperture of all the samples proved to consume too much time. Characterization of fracture aperture in layered samples can be improved by thoroughly measuring it throughout the sample.

Bibliography

- Anderson, E. M. (1951). *The dynamics of faulting and dyke formation with applications to Britain*. Oliver and Boyd, Edinburgh.
- ASTM D2938-95 (1995). Standard test method for unconfined compressive strength of intact rock core specimens. Standard, American Society for Testing and Materials, West Conshohocken PA.
- ASTM D3148-96 (1996). Standard test method for elastic moduli of intact rock core specimens in uniaxial compression. Standard, American Society for Testing and Materials, West Conshohocken PA.
- Brenner, S. L. and Gudmundsson, A. (2004). Arrest and aperture variation of hydrofractures in layered reservoirs. *Geological Society of London, Special Publications*, 231(1):117–128.
- Cooke, M. L., Simo, J. A., Underwood, C. A., and Rijken, P. (2006). Mechanical stratigraphic controls on fracture patterns within carbonates and implications for groundwater flow. *Sedimentary Geology*, 184:225–239.
- Cooke, M. L. and Underwood, C. A. (2001). Fracture termination and step-over at bedding interfaces due to frictional slip and interface opening. *Journal of Structural Geology*, 23:223–238.
- Dunham, K. (1948). *Geology of the northern Pennine orefield, Volume 1: Tyne to Stainmore*. HMSO, London.
- Ferrill, D. A., McGinnis, R. N., Morris, A. P., Smart, K. J., Sickmann, Z. T., Bentz, M., Lehrmann, D., and Evans, M. A. (2014). Control of mechanical stratigraphy on bed-restricted jointing and normal faulting: Eagle ford formation, south-central Texas. *AAPG Bulletin*, 98(11):2477–2506.
- Ferrill, D. A. and Morris, A. P. (2003). Dilational normal faults. *Journal of Structural Geology*, 25:183–196.
- Ferrill, D. A., Morris, A. P., McGinnis, R. N., Smart, K. J., and Wigginton, S. S. (2017). Mechanical stratigraphy and normal faulting. *Journal of Structural Geology*, 94:275–302.
- Fossen, H. (2010). *Structural Geology*. Cambridge University Press.
- Gillespie, P. A., Johnston, J. D., Loriga, M. A., McCaffrey, K. J. W., Walsh, J. J., and Watterson, J. (1999). Influence of layering on vein systematics in line samples. *Geological Society of London, Special Publications*, 155:35–56.
- Gross, M. R. and Eyal, Y. (2007). Throughgoing fractures in layered carbonate rocks. *GSA Bulletin*, 119(11/12):1387–1404.
- Gudmundsson, A. (2002). Emplacement and arrest of sheets and dykes in central volcanoes. *Journal of Volcanology and Geothermal Research*, 116:279–298.
- Gudmundsson, A. (2011). *Rock Fractures in Geological Processes*. Cambridge University Press, Cambridge, United Kingdom.
- Gudmundsson, A. and Brenner, S. L. (2001). How hydrofractures become arrested. *Terra Nova*, 13:456–462.
- Haimson, B. and Chang, C. (2000). A new true triaxial cell for testing mechanical properties of rock, and its use to determine rock strength and deformability of westerly granite. *International Journal of Rock Mechanics and Mining Sciences*, 37:285–296.
- Handin, J., Hager, R. V., Friedman, M., and Feather, J. N. (1963). Experimental deformation of sedimentary rocks under confining pressure: Pore pressure tests. *AAPG Bulletin*, 47(5):717–755.
- Hoek, E. and Franklin, J. (1968). Simple triaxial cell for field or laboratory testing of rock. *Transactions of the Institution of Mining and Metallurgy*, 77:A22–A26.

- Hoek, E. and Martin, C. D. (2014). Fracture initiation and propagation in intact rock - a review. *Journal of Rock Mechanics and Geotechnical Engineering*, 6:287–300.
- ISRM (1978). Suggested methods for determining tensile strength of rock materials. *International Journal of Rock Mechanics and Mining Sciences & Geomechanics Abstracts*, 15(3).
- Janmahomed, F. R. (2016). An experimental investigation on the rock mechanical behavior of synthetic layered systems and load-cycling of its individual constituents. Master's thesis, Delft University of Technology, Delft, The Netherlands.
- Mavko, G., Mukerji, T., and Dvorkin, J. (2003). *The Rock Physics Handbook: Tools for Seismic Analysis in Porous Media*. Cambridge University Press, Cambridge, United Kingdom.
- McGinnis, R. N., Ferrill, D. A., Morris, A. P., Smart, K. J., and Lehrmann, D. (2017). Mechanical stratigraphic controls on natural fracture spacing and penetration. *Journal of Structural Geology*, 95:160–170.
- McGinnis, R. N., Ferrill, D. A., Smart, K. J., Morris, A. P., Higuera-Diaz, C., and Prawica, D. (2015). Pitfalls of using entrenched fracture relationships: Fractures in bedded carbonates of the hidden valley fault zone, canyon lake gorge, comal county, texas. *AAPG Bulletin*, 99(12):2221–2245.
- Michelis, P. (1985). A true triaxial cell for low and high pressure experiments. *International Journal of Rock Mechanics and Mining Sciences and Geomechanics*, 22(3):183–188.
- Morris, A. P., Ferrill, D. A., and McGinnis, R. N. (2009). Mechanical stratigraphy and faulting in cretaceous carbonates. *AAPG Bulletin*, 93(11):1459–1470.
- Olson, J. E. (2007). Fracture aperture, length and pattern geometry development under biaxial loading: a numerical study with applications to natural, cross-jointed systems. *Geological Society of London, Special Publications*, 289:123–142.
- Olson, J. E., Laubach, S. E., and Lander, R. H. (2009). Natural fracture characterization in tight gas sandstones: Integrating mechanics and diagenesis. *AAPG Bulletin*, 93(11):1535–1549.
- Passey, Q., Bohacs, K., Esch, W., Klimentidis, R., and Sinha, S. (2010). From oil-prone source rock to gas-producing shale reservoir - geologic and petrophysical characterization of unconventional shale-gas reservoirs. In *CPS/SPE International Oil & Gas Conference and Exhibition*, Beijing, China.
- Roche, V., Homberg, C., and Rocher, M. (2012). Architecture and growth of normal fault zones in multilayer systems: A 3d field analysis in the south-eastern basin, france. *Journal of Structural Geology*, 37:19–35.
- Schöpfer, M. P. J., Childs, C., Walsh, J. J., Manzocchi, T., and Koyi, H. A. (2007). Geometrical analysis of the refraction and segmentation of normal faults in periodically layered systems. *Journal of Structural Geology*, 29:318–335.
- Teufel, L. W. and Clark, J. A. (1984). Hydraulic fracture propagation in layered rock: Experimental studies of fracture containment. *Society of Petroleum Engineers Journal*, 24(1):19–32.
- Underwood, C. A., Cooke, M. L., Simo, J. A., and Muldoon, M. A. (2003). Stratigraphic controls on vertical fracture patterns in silurian dolomite, northeastern wisconsin. *AAPG Bulletin*, 87(1):121–142.
- Unknown (2012). Cover image: Fractures at checkerboard mesa, zion national park. <https://travelintheusa.files.wordpress.com/2012/08/sdc12580.jpg>.
- Vernik, L. and Zoback, M. D. (1992). Estimation of maximum horizontal principal stress magnitude from stress-induced well bore breakouts in the cajon pass scientific research borehole. *Journal of Geophysical Research*, 97(B4):5109–5119.
- Volume Graphics (2017). myvgl 3.0 sp4. <https://www.volumegraphics.com/en/products/myvgl.html>.
- Wellington, S. L. and Vinegar, H. J. (1987). X-ray computerized tomography. *Journal of Petroleum Technology*, 39(08).
- Wen, Z., Huang, G., and Zhan, H. (2006). Non-darcian flow in a single confined vertical fracture toward a well. *Journal of Hydrology*, 330(3):698–708.
- Zoback, M. D. (2007). *Reservoir Geomechanics*. Cambridge University Press.
- Zotz-Wilson, R. D. (2016). Bentheim and granite dataset. not published.

Appendices

Appendix A

List of experiments

Sample	Layer 1	Layer 2	Layer 3	Confining pressure (MPa)	Ultimate Strength (MPa)
L1	BNT	BNT	BNT	30	179
L2	BNT	GRA	BNT	30	185
L3	AIN	AIN	AIN	30	367
L4	IND	BNT	IND	30	-
L5	BNT	IND	BNT	30	-
L6	GRA	BNT	GRA	30	180
L7	BNT	GRA	BNT	30	196
L8	RF	YF	RF	30	172
L9	GRA	AIN	GRA	30	388
L10	AIN	GRA	AIN	30	375
L11	RF	YF	RF	15	116.5
L12	BNT	GRA	BNT	15	127
L13	AIN	GRA	AIN	15	285
L14	BNT	IND	BNT	15	88
L15	AIN	BNT	AIN	15	144.5
L16	AIN	BNT	AIN	0	38.5
L17	AIN	BNT	AIN	10	117
L18	RF	YF	RF	10	102.5
L19	AIN	BNT	AIN	40	215.5
L20	RF	BNT	RF	40	216.1
L21	AIN	BNT	AIN	50	241.3
L22	RF	BNT	RF	50	241
L26	AIN	GRA	AIN	40	389
L27	AIN	SLT	AIN	0	14.8
L28	AIN	GRA	AIN	0	176
L29	AIN	BNT	AIN	30	189.2
L30	RF	GRA	RF	0	51.4
L31	RF	GRA	RF	10	132.5
L32	RF	GRA	RF	15	149
L33	RF	BNT	RF	0	23.7
L34	RF	BNT	RF	30	181.9
L35	BER	BNT	BER	20	151.4
L36	BER	BNT	BER	30	195
L37	BER	BNT	BER	15	140
L38	BER	BNT	BER	20	147.3
L39	BER	BNT	BER	10	127.3
L40	RF	GRA	RF	10	111.5
L41	BER	BNT	BER	40	208
L42	BER	BNT	BER	0	39
L43	AIN	GRA	AIN	40	434
L44	SLT	GRA	SLT	0	18.6
L45	BNT	GRA	BNT	20	155
2N	BNT	GRA	BNT	0	53

Table 4: List of all layered experiments. BNT: Bentheim sandstone, BER: Beringen sandstone, AIN: Ainsa sandstone, RF: Red Felser sandstone, GRA: Bism granite, SLT: Huesca siltstone, YF: Yellow Felser sandstone.

Sample	Material	Confining pressure (MPa)	Ultimate Strength (MPa)
A10	YF	20	146.3
A6	YF	10	111.1
A7	YF	15	126.5
B1	RF	0	36.8
B2	RF	10	113.7
B3	RF	15	146.8
B4	RF	20	169
B5	RF	30	212
B6	RF	20	175.6
B7	RF	0	19.4
B8	RF	0	19.2
B9	RF	0	19
B20	RF	0	28
B21	RF	0	31.5
B22	RF	0	29.2
C1	BER	10	223.6
C2	BER	0	121.8
C3	BER	15	250.3
C4	BER	0	102
C5	BER	0	141.7
C6	BER	0	135
C7	BER	0	128
D1	AIN	10	244
D2	AIN	0	154.1
D3	AIN	20	303.5
D4	AIN	30	345.7
D5	AIN	40	361.4
D6	AIN	0	69.7
D7	AIN	0	84.3
D8	AIN	0	76.5
E1	AIN	10	271
E2	AIN	0	190.5
E3	AIN	20	297
E4	AIN	30	350
E5	AIN	40	382.5
E6	AIN	0	217.5
E7	AIN	30	305.8
E10	AIN	0	195
E11	AIN	0	208
E12	AIN	0	206.5
BNT1	BNT	0	42.5
BNT2	BNT	0	42
BNT3	BNT	0	33.2
BNT4	BNT	0	43.7
GRA1	GRA	0	237
GRA2	GRA	0	207.2
SLT1	SLT	0	13

Table 5: List of all monophasic experiments. BNT: Bentheim sandstone, BER: Beringen sandstone, AIN: Ainsa sandstone, RF: Red Felser sandstone, GRA: Benin granite, SLT: Huesca siltstone, YF: Yellow Felser sandstone.

Appendix B

Fracture orientation change

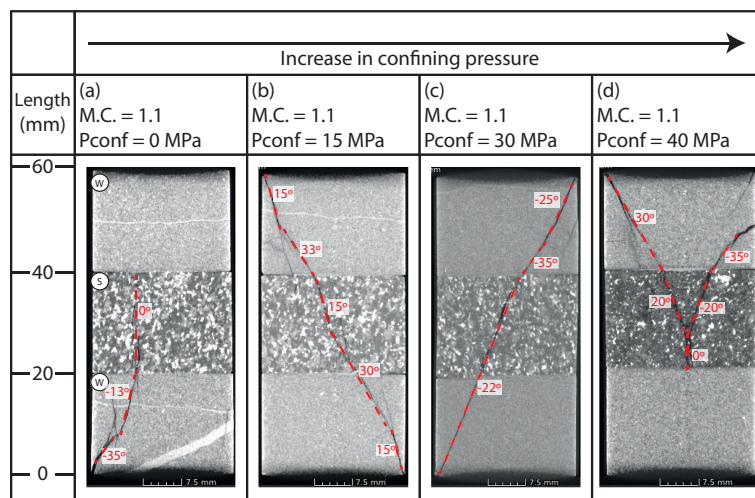


Figure 36: Micro-CT slices of fracture propagation with annotated fracture orientation for increasing confining pressures. Samples consist of Ainsa sandstone and Benin granite. Mechanical contrast between both types of rock is 1.1.

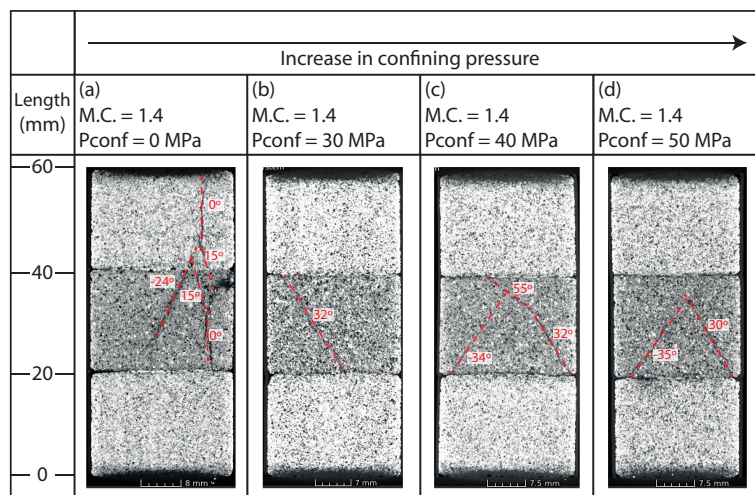


Figure 37: Micro-CT slices of fracture propagation with annotated fracture orientation for increasing confining pressures. Samples consist of Red Felser sandstone and Bentheim sandstone. Mechanical contrast between both types of rock is 1.4.

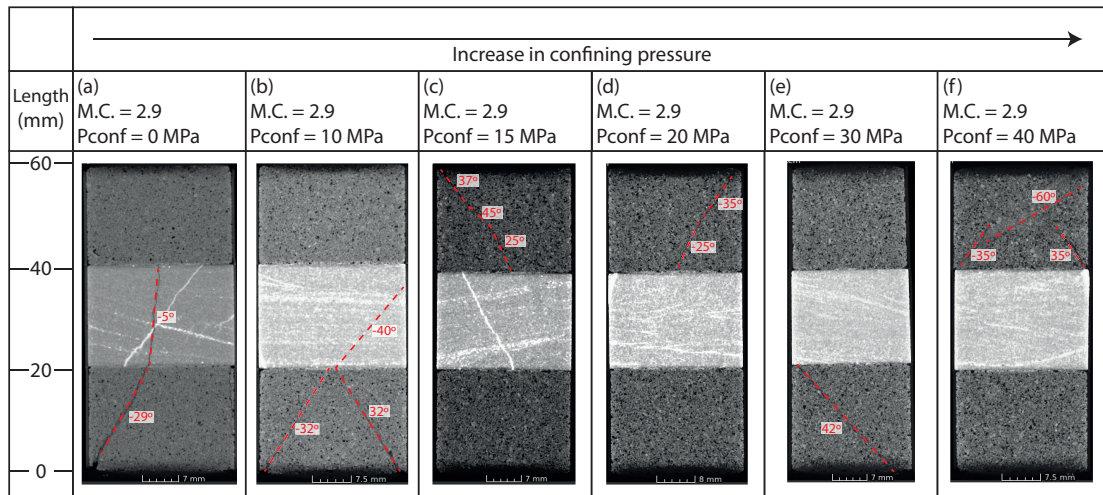


Figure 38: Micro-CT slices of fracture propagation with annotated fracture orientation for increasing confining pressures. Samples consist of Bentheim sandstone and Beringen sandstone. Mechanical contrast between both types of rock is 2.9.

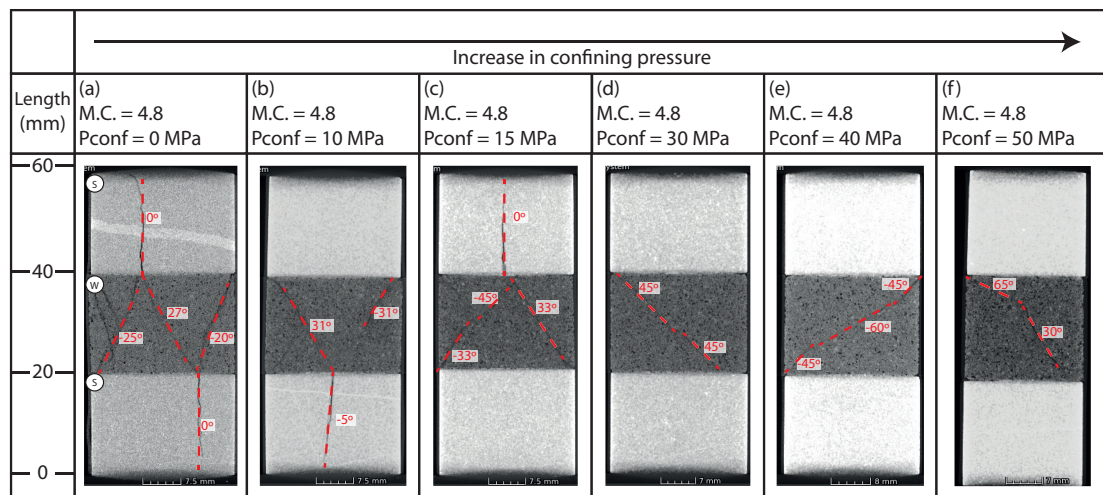


Figure 39: Micro-CT slices of fracture propagation with annotated fracture orientation for increasing confining pressures. Samples consist of Ainsa sandstone and Bentheim sandstone. Mechanical contrast between both types of rock is 4.8.

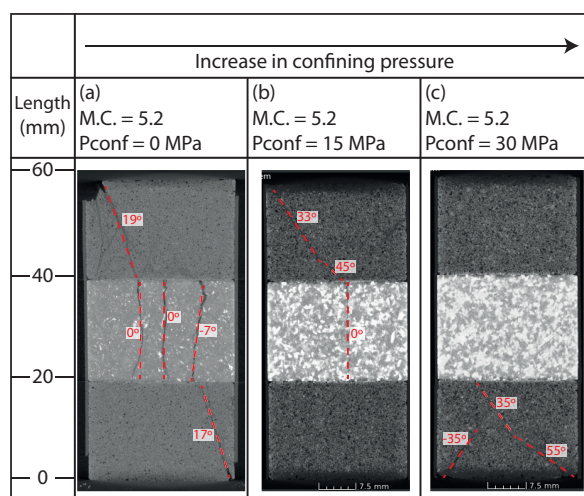


Figure 40: Micro-CT slices of fracture propagation with annotated fracture orientation for increasing confining pressures. Samples consist of Bentheim sandstone and Benin granite. Mechanical contrast between both types of rock is 5.2.

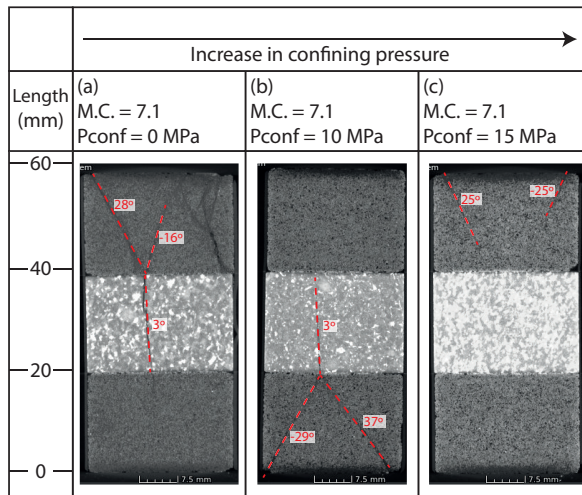


Figure 41: Micro-CT slices of fracture propagation with annotated fracture orientation for increasing confining pressures. Samples consist of Red Felser sandstone and Benin granite. Mechanical contrast between both types of rock is 7.1.

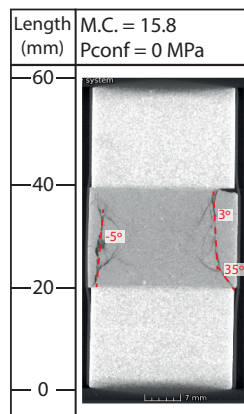


Figure 42: Micro-CT slice of fracture propagation with annotated fracture orientation at unconfined pressure conditions. Sample consists of Ainsa sandstone and Huesca siltstone. Mechanical contrast between both types of rock is 15.8.

Appendix C

Ultrasonic travelttime measurements

Bentheim sandstone				
Length (mm)	P-wave time (us)	S-wave time (us)	P-wave velocity (m/s)	S-wave velocity (m/s)
20.72	8.95	12.80	2315	1618
20.13	8.50	12.40	2369	1624
20.30	8.75	12.45	2320	1631
20.62	8.90	12.50	2316	1649
20.53	8.85	12.55	2320	1636
17.75	7.65	12.15	2320	1461
20.40	9.15	13.00	2230	1569
19.28	8.15	12.45	2366	1549
20.15	9.45	12.95	2132	1556
20.00	8.30	12.15	2410	1646
20.13	8.80	12.85	2288	1567
19.43	8.10	11.70	2399	1661
Average			2315	1597
St. Dev.			76	58

Table 6: Ultrasonic travelttime measurements and ultrasonic velocities through Bentheim sandstone samples.

Yellow Felser sandstone				
Length (mm)	P-wave time (us)	S-wave time (us)	P-wave velocity (m/s)	S-wave velocity (m/s)
33.37	10.90	15.00	3061	2224
33.00	11.05	15.20	2986	2171
19.23	6.60	8.95	2914	2149
20.63	7.10	10.50	2906	1965
20.53	7.25	10.80	2832	1901
18.40	6.40	9.60	2875	1917
Average			2929	2055
St. Dev.			82	143

Table 7: Ultrasonic travelttime measurements and ultrasonic velocities through Yellow Felser sandstone samples.

Red Felser sandstone				
Length (mm)	P-wave time (us)	S-wave time (us)	P-wave velocity (m/s)	S-wave velocity (m/s)
33.72	13.80	21.70	2443	1554
33.15	14.30	21.10	2318	1571
19.72	8.65	13.45	2279	1466
20.42	9.25	13.55	2207	1507
19.68	9.55	14.45	2061	1362
20.28	8.45	12.60	2400	1610
19.95	8.50	12.80	2347	1559
20.13	9.00	13.35	2237	1508
19.82	9.00	12.95	2202	1530
Average			2277	1518
St. Dev.			116	72

Table 8: Ultrasonic travelttime measurements and ultrasonic velocities through Red Felser sandstone samples.

Ainsa sandstone				
Length (mm)	P-wave time (us)	S-wave time (us)	P-wave velocity (m/s)	S-wave velocity (m/s)
59.85	11.95	19.25	5008	3109
59.95	12.15	19.45	4934	3082
59.65	12.10	19.10	4930	3123
59.95	12.15	19.15	4934	3131
60.20	12.15	19.65	4955	3064
60.00	12.00	19.15	5000	3133
Average			4960	3107
St. Dev.			35	28

Table 9: Ultrasonic travelttime measurements and ultrasonic velocities through Ainsa sandstone samples.

Fontainebleau sandstone				
Length (mm)	P-wave time (us)	S-wave time (us)	P-wave velocity (m/s)	S-wave velocity (m/s)
20.30	5.40	9.65	3759	2104
20.98	8.70	13.70	2412	1532
21.03	5.65	8.30	3723	2534
21.02	6.00	9.75	3503	2156
19.85	8.65	11.70	2295	1697
21.00	6.00	7.85	3500	2675
20.38	5.10	8.90	3997	2290
21.32	7.10	13.40	3002	1591
21.30	5.70	9.65	3737	2207
20.00	5.70	9.70	3509	2062
20.97	6.30	11.60	3328	1807
20.75	8.35	11.10	2485	1869
20.70	5.25	7.75	3943	2671
20.70	5.20	7.10	3981	2915
20.80	5.40	7.40	3852	2811
Average			3402	2195
St. Dev.			584	449

Table 10: Ultrasonic travelttime measurements and ultrasonic velocities through Fontainebleau sandstone samples.

Benin granite				
Length (mm)	P-wave time (us)	S-wave time (us)	P-wave velocity (m/s)	S-wave velocity (m/s)
19.88	3.90	6.10	5098	3260
20.82	4.14	6.40	5028	3253
15.93	3.88	5.68	4107	2805
19.18	3.86	5.62	4970	3413
20.10	4.08	6.28	4926	3201
19.85	4.00	6.28	4963	3161
Average			4849	3182
St. Dev.			369	204

Table 11: Ultrasonic traveltime measurements and ultrasonic velocities through Benin granite samples.

Appendix D

Brazilian tensile strength

Bentheimer sandstone				
Sample	Height (mm)	Diameter (mm)	Peak load (kN)	BTS (MPa)
1	15.50	29.80	1.8355	2.53
2	15.57	29.80	2.7862	3.82
3	15.98	29.80	2.4468	3.27
4	15.77	29.80	2.5594	3.47
5	15.35	29.80	2.2515	3.13
6	15.35	29.80	1.9975	2.78
Average			2.31	3.17
St. Dev.			0.36	0.47

Table 12: Brazilian disc test results of Bentheimer sandstone samples.

Yellow Felser sandstone				
Sample	Height (mm)	Diameter (mm)	Peak load (kN)	BTS (MPa)
1	16.25	29.80	4.8017	6.31
2	15.80	29.80	4.7023	6.36
3	15.40	29.80	4.3165	5.99
4	15.48	29.80	4.5381	6.26
5	15.40	29.80	4.8985	6.80
6	14.90	29.80	3.9865	5.72
Average			4.54	6.24
St. Dev.			0.34	0.37

Table 13: Brazilian disc test results of Yellow Felser sandstone samples.

Red Felser sandstone				
Sample	Height (mm)	Diameter (mm)	Peak load (kN)	BTS (MPa)
1	15.85	29.85	2.0892	2.81
2	15.10	29.85	1.9697	2.78
3	15.52	29.85	1.4710	2.02
4	15.50	29.85	1.8405	2.53
5	15.62	29.85	1.6803	2.30
6	15.75	29.85	1.7326	2.35
Average			1.80	2.46
St. Dev.			0.22	0.30

Table 14: Brazilian disc test results of Red Felser sandstone.

Ainsa D sandstone				
Sample	Height (mm)	Diameter (mm)	Peak load (kN)	BTS (MPa)
1	16.10	29.75	9.3658	12.45
2	15.40	29.75	13.8939	19.31
3	15.45	29.75	12.4202	17.20
4	15.95	29.75	12.2291	16.41
5	15.63	29.75	13.8826	19.00
6	15.68	29.75	14.3287	19.55
Average			12.69	17.32
St. Dev.			1.84	2.70

Table 15: Brazilian disc test results of Ainsa D sandstone.

Ainsa E sandstone				
Sample	Height (mm)	Diameter (mm)	Peak load (kN)	BTS (MPa)
1	15.08	29.80	11.7387	16.63
2	15.92	29.80	12.4461	16.70
3	15.83	29.80	11.1651	15.06
4	15.73	29.80	9.4885	12.88
5	15.23	29.80	9.6263	13.50
6	16.25	29.80	11.3849	14.97
Average			10.97	14.96
St. Dev.			1.18	1.57

Table 16: Brazilian disc test results of Ainsa E sandstone.